Draft version February 19, 2024
Preprint typeset using LaTeX style emulateapj v. 12/16/11

THE REGULATION OF GALAXY GROWTH ALONG THE SIZE-MASS RELATION BY STAR-FORMATION, AS TRACED BY Hα IN KMOS^{3D} GALAXIES AT $0.7 \lesssim z \lesssim 2.7$ †

David J. Wilman[1,2], Matteo Fossati[3,2,1,‡], J. Trevor Mendel[4,5,2], Roberto Saglia[2,1], Emily Wisnioski[4,5,2], Stijn Wuyts[6,2], Natascha Förster Schreiber[2], Alessandra Beifiori[1,2], Ralf Bender[1,2], Sirio Belli[2], Hannah Übler[2], Philipp Lang[7,2], Jeffrey C.C. Chan[8,2], Rebecca L. Davies[2], Erica J. Nelson[9,2], Reinhard Genzel[2], Linda J. Tacconi[2], Audrey Galametz[10,2], Richard I. Davies[2], Dieter Lutz[2], Sedona Price[2], Andreas Burkert[1,2], Ken-ichi Tadaki[11,2], Rodrigo Herrera-Camus[12,2], Gabriel Brammer[13], Ivelina Momcheva[14], Pieter van Dokkum[15]

Draft version February 19, 2024

ABSTRACT

We present half-light sizes measured from Hα emission tracing star-formation in 281 star-forming galaxies from the KMOS^{3D} survey at $0.7 \lesssim z \lesssim 2.7$. Sizes are derived by fitting 2D exponential disk models, with bootstrap errors averaging 20%. Hα sizes are a median (mean) of 1.19 (1.26) times larger than those of the stellar continuum – which due to radial dust gradients places an upper limit on the growth in stellar size via star formation – with just $\sim 43\%$ intrinsic scatter. At fixed continuum size the Hα size shows no residual trend with stellar mass, star formation rate, redshift or morphology. The only significant residual trend is with the excess obscuration of Hα by dust, at fixed continuum obscuration. The scatter in continuum size at fixed stellar mass is likely driven by the scatter in halo spin parameters. The stability of the ratio of Hα size to continuum size demonstrates a high degree of stability in halo spin and in the transfer of angular momentum to the disk over a wide range of physical conditions and cosmic time. This may require local regulation by feedback processes. The implication of our results, as we demonstrate using a toy model, is that our upper limit on star-formation driven growth is sufficient only to evolve star-forming galaxies approximately *along* the observed size-mass relation, consistent with the size growth of galaxies at constant cumulative co-moving number density. To explain the observed evolution of the size-mass relation of star-forming disk galaxies other processes, such as the preferential quenching of compact galaxies or galaxy mergers, may be required.

Keywords: galaxies: evolution, galaxies: structure, galaxies: star-formation, techniques: imaging spectroscopy

† Based on observations obtained at the Very Large Telescope (VLT) of the European Southern Observatory (ESO), Paranal, Chile (ESO program IDs 092.A-0091, 093.A-0079, 094.A-0217, 095.A-0047, 096.A-0025, 097.A-0028, 098.A-0045, 099.A-0013

[1] Universitäts-Sternwarte München, Scheinerstrasse 1, 81679 München, Germany
[2] Max-Planck-Insitut für extraterrestrische Physik, Giessenbachstrasse, 85748 Garching, Germany
[3] Centre for Extragalactic Astronomy and Institute for Computational Cosmology, Durham University, South Road, Durham, DH1 3LE, UK
[4] Research School of Astronomy and Astrophysics, Australian National University, Canberra, ACT 2611, Australia
[5] 3ARC Centre of Excellence for All Sky Astrophysics in 3 Dimensions (ASTRO 3D)
[6] Department of Physics, University of Bath, Claverton Down, Bath, BA2 7AY, UK
[7] Max Planck Institute for Astronomy (MPIA), Königstuhl 17, D-69117, Heidelberg, Germany
[8] Department of Physics and Astronomy, University of California Riverside, 900 University Avenue, Riverside, CA 92521, USA
[9] Harvard-Smithsonian Center for Astrophysics, 60 Garden St, Cambridge, MA 02138
[10] Observatoire de Genve, Universit de Genve, 51 Ch. des Maillettes, CH-1290 Versoix, Switzerland
[11] National Astronomical Observatory of Japan, 2-21-1 Osawa, Mitaka, Tokyo 181-8588, Japan 0000-0001-9728-8909
[12] Astronomy Department, Universidad de Concepción, Barrio Universitario, Concepción, Chile
[13] Cosmic Dawn Center, Niels Bohr Institute, University of Copenhagen, Juliane Maries Vej 30, DK-2100 Copenhagen, Denmark
[14] Space Telescope Science Institute, Baltimore, MD, United States
[15] Astronomy Department, Yale University, 52 Hillhouse Avenue, New Haven, CT 06511, USA
‡ email: matteo.fossati@durham.ac.uk

1. INTRODUCTION

Most star-forming galaxies in the Universe above stellar masses of $M_* \sim 10^9\,M_\odot$ have most of their stars in disks (e.g. van der Wel et al. 2014a; Wuyts et al. 2011). These are stable, rotationally-supported structures which, in the absence of dramatic events such as major mergers, survive at least for the Hubble time with disk galaxies still dominant in the local star-forming population. Galaxy disks typically have radial surface brightness profiles well described by a declining exponential function (although an improved description of many local stellar disks is a broken exponential law, becoming either steeper or more shallow beyond a break radius, Erwin, Pohlen & Beckman 2008). Disks exist not only in the stellar component but also in the gas which feeds them and, although the thickness of stellar disks and turbulence in gas disks can vary with time, basic disk structures with dominant rotational support exist to high redshifts (e.g. Genzel et al. 2006; Förster Schreiber et al. 2006, 2009; Kassin et al. 2012; Livermore et al. 2015), up to at least $z \sim 3$ (Turner et al. 2017), and are dominant among the high mass population by $z \sim 2.2$ (Wisnioski et al. 2015; Stott et al. 2016), with evidence that they are common even in the most compact (Wisnioski et al. 2018) and passively evolving old galaxies at that redshift (e.g. McGrath et al. 2008; van der Wel et al. 2011; Chang et al. 2013; Newman, Belli & Ellis 2015; Toft et al. 2017; Hill et al. 2019).

The structure of massive star-forming galaxies is made not only of rotating disks but also by central dispersion dominated bulges (Lang et al. 2014). These could be the result of violent star formation from low angular momentum cold gas in the center of galaxies, although they can also form during merger events. Submillimeter observations reveal very high rates of highly obscured star-formation at the centre of massive galaxies at high redshift (Tadaki et al. 2017). Such events appear to coexist with more extended and less obscured star formation (e.g. Chen et al. 2017), such that star-forming disks tend to retain an exponential profile, even in the presence of a bulge or bar.

Observations in the local Universe indicate that stars form predominantly from the dense and cool molecular gas component, with star-formation surface density well correlated to the molecular gas surface density (Bigiel et al. 2008), with a slope close to unity in the disk regime, implying a constant timescale for the depletion of molecular gas by star-formation. Interestingly, the star-formation also appears to track the existing stars, to first order. For example, there exists a relation between the local density of star-formation and that of stars (González Delgado et al. 2016). This reflects on the spatial extent of these components, such that in terms of half-light sizes, the size of the star-forming disks are found to be extremely similar to that of the stellar disk in the local Universe (Fossati et al. 2013).

As gas accretes onto a galaxy it still carries much of the angular momentum from the cosmic filaments which feed the galaxy and its halo (Fall & Romanowsky 2018). Smooth accretion of gas with a consistent axis of angular momentum leads to the formation of gas disks. While the mean specific angular momentum of disks is similar to that of their halo (Burkert et al. 2016), the distribution within any single galaxy of angular momentum from newly accreted halo gas is expected to extend to both lower and higher values than found in typical galaxy disks (e.g. Dalcanton, Spergel & Summers 1997; van den Bosch 2001; Dutton 2009). The high angular momentum material can be transported to large radii where it will exist in a diffuse atomic or ionized component unable to form new stars, while the low angular momentum material can be removed in energetic supernovae-driven winds. Such winds are particularly effective at removing material from low mass and compact galaxies (Dutton 2009) but can be delay the evolution of higher mass galaxies via high redshift ejection and re-incorporation (e.g. Hirschmann et al. 2013).

The existence at $0 < z \lesssim 3$ of a Main Sequence (MS) of star-formation, relating the galaxy star-formation rate (SFR) to the stellar mass with a small scatter (~ 0.3 dex, e.g. Noeske et al. 2007; Whitaker et al. 2014; Schreiber et al. 2015; Gavazzi et al. 2015) implies that the combined processes of gas accretion and star-formation must be smooth and stable over the relatively short timescales to which we are sensitive with typical star-formation indicators. Moreover these small variations in star-formation rate at fixed stellar mass seem to have no measurable dependence on the galaxy size, but are rather driven by the molecular content of galaxies or its depletion rate (Saintonge et al. 2011; Tacconi et al. 2018). The mass of the cold gas reservoir is also the main driver of the cosmic evolution of the star formation activity, with gas rich galaxies at $z \sim 1-2$, forming stars much more rapidly than in the local Universe (Madau & Dickinson 2014; Whitaker et al. 2014).

The relationship between the local density of star formation and of stellar mass found in the local Universe appears to extend to at least $z \sim 1$ (Wuyts et al. 2013). Half-light sizes in the Hα emission line tracing unobscured star-formation are similar to or slightly larger than the size in continuum light in both individual highly star-forming galaxies (Nelson et al. 2012) and in the stacked averages for normally star-forming galaxies (Nelson et al. 2016a). Using 3D-HST slitless spectroscopic data (van Dokkum et al. 2011; Brammer et al. 2012; Skelton et al. 2014; Momcheva et al. 2016), Nelson et al. (2016a) show that the stacked average Hα profiles of star-forming galaxies with higher or lower than normal SFR for their stellar mass are self-similar, changing only in normalization and not half-light size. The sizes of molecular gas disks themselves are not easily measured at high redshift in normally star-forming galaxies. Where measured, they appear similar in extent to the stellar or star-forming disks (Tacconi et al. 2013; Bolatto et al. 2015) while in the highly star-forming, high mass population the situation is more complex: highly compact dust emission can co-exist with more extended emission from tracers of molecular gas such as CO (Calistro Rivera et al. 2018).

KMOS^{3D} is a unique 75 night guaranteed time program with the ESO Very Large Telescope (VLT) with the second generation instrument KMOS (K-band Multi-Object Spectrograph, Sharples12,14) targeting the Hα+[NII] emission line complex in ~ 740 galaxies selected to have a magnitude Ks < 23 and in the range $0.7 \lesssim$ z $\lesssim 2.7$ (Wisnioski et al. 2019, – hereafter W19 –, Wisnioski

et al. 2015). The multiplexing capabilities of KMOS allow us to target more galaxies and with deeper observations than was possible with single object IFUs such as SINFONI (e.g. the SINS survey Förster Schreiber et al. 2009), and compliments contemporary work on smaller numbers of objects featuring the high spatial resolution available with adaptive optics (e.g. Förster Schreiber et al. 2018).

In this paper we use KMOS^{3D} data to map Hα and measure Hα disk sizes in individual star-forming galaxies across a wide range in redshift and SFR. We examine whether the stacked results of Nelson et al. (2016a) apply for individual galaxies, whether size growth via star-formation is correlated with the stellar mass and star-formation rate or is driven by other fundamental parameters. across a wide baseline in redshift including the peak of the cosmic star formation activity. KMOS^{3D} offers several advantages compared to 3D-HST for a study of this nature: it is significantly deeper, its spectral resolution allows us to resolve the Hα + [NII] emission line complex, and observations in the YJ to Ks band allow us to trace Hα emission over a larger redshift range. Being a seeing-limited ground-based survey, this goes at the expense of spatial resolution.

Following our brief introduction to the KMOS^{3D} survey in Section 2, Sections 3 to 5 give a detailed account of how we go from raw KMOS data to accurate size measurements of KMOS^{3D} galaxies with well calibrated errors. Readers primarily interested in our results on – and interpretation of – the size growth of star-forming galaxies may skip to Section 6. For readers interested in the technical steps, we describe the basic data reduction in Section 3 and the generation of Hα maps and profiles in Section 4. In Section 5 we describe the flagging procedures used to verify our sample and show that it is not biased with respect to normally star-forming MS galaxies. We also release to the community the size measurements derived in this work. We then examine which parameters control the Hα size of KMOS^{3D} galaxies in Section 6 and in Section 7 discuss what this means for our understanding of how galaxies grow in size through star-formation. Our key conclusions are presented in Section 8. Throughout this paper we assume a flat ΛCDM cosmology with $H_0 = 70\,\mathrm{km\,s^{-1}\,Mpc^{-1}}$, $\Omega_m = 0.3$ and $\Omega_\Lambda = 0.7$.

2. THE KMOS^{3D} SURVEY

KMOS^{3D} takes advantage of the unique multiplexing and spatially-resolved near infrared (NIR) spectroscopic capabilities of KMOS as well as the large collecting area of the 8.2 m VLT mirror, targeting the Hα+[NII] emission line complex in galaxies at $0.7 \lesssim z \lesssim 2.7$. This provides simultaneous flux and kinematic maps of the ionized gas for up to 24 galaxies in one exposure by deploying 24 configurable arms in the 7.2′ field of view, each hosting a $2.8 \times 2.8''$ integral field unit (IFU).

The first year of the KMOS^{3D} survey was described by (Wisnioski et al. 2015). KMOS^{3D} targets galaxies selected from the 3D-HST grism (Brammer et al. 2012; Skelton et al. 2014; Momcheva et al. 2016) and CANDELS imaging (Grogin et al. 2011; Koekemoer et al. 2011) surveys with the Hubble Space Telescope (HST) in the COSMOS, GOODS-South and UDS deep fields accessible from Paranal. Targets are selected to have a magnitude Ks < 23, and a known spectroscopic or grism redshift (grism redshifts from 3D-HST have an accuracy of $\approx 1000\,\mathrm{km\,s^{-1}}$ Momcheva et al. 2016; Fossati et al. 2017) for which the spectrum around Hα should be relatively free of atmospheric OH lines, and visible in the KMOS YJ, H or K-bands. We apply no prior selection on star formation rate or Hα flux in order to avoid selection bias and sample the full range of galaxies down to our detection limits. Due to the unique multiplexing capabilities of KMOS, we are able to observe galaxies from $\sim 3-30$ hours by re-targeting objects with weak detections to improve the signal to noise ratio.

Observations for KMOS^{3D} were carried out from October 2013 until April 2018 following an object-sky-object (OSO) observation pattern such that each object exposure is adjacent to a sky exposure in the same IFU. Three IFUs were placed on stars to trace the variable spatial Point Spread Function (PSF) and throughput from exposure to exposure, leading to a simultaneous observations of up to 21 galaxies per exposure.

In this work we consider all data taken up until April 2017, comprising 645 galaxies targeted for observations of Hα and [NII]. Data were taken in a range of observing conditions, with PSF minor axis FWHM ranging between 0.3″ and 0.92″ and a median of 0.456″. The final KMOS3D data set is fully described in (W19). Star-formation rates (SFR) used in this paper are computed using the data and method described by Wuyts et al. (2011), based on infrared, UV and optical observations and thus independent of our Hα measurements.

3. DATA REDUCTION

Our reductions in this paper are intermediate between the early data reduction described by Wisnioski et al. (2015) and that described in the data release paper (W19). We refer to W19 for much of the reduction procedure noting where implementation of specific steps differ. In particular we describe in detail the steps which optimise the background subtraction and astrometry, and which were tailored to allow a robust extraction of Hα profiles and sizes of galaxies.

3.1. *Basic reduction*

All our basic calibration steps, with the exception of the sky and background subtraction, are identical to those described by W19. We make use of the Software Package for Astronomical Reductions with KMOS (SPARK) code which works within the ESO pipeline execution tool (ESOREX), supplemented with some custom tools written in the IDL and PYTHON languages. This includes masking of bad pixels and flattening at the detector level; reconstruction of data cubes including a refined wavelength calibration using sky lines and a heliocentric correction; followed by a correction for the spatial illumination uniformity, and flux calibration using standard star observations. During this last step we used the flux from stars observed in the same setup as the galaxies to correct for frame to frame variations in the throughput. Bad frames are inspected and removed. Skyline subtraction was applied using the standard method in SPARK which subtracts an adjacent sky frame with skylines scaled to optimally match the science observation (Davies 2007).

Once individual frames are generated. it is essential to subtract a residual background level per frame: not doing so results in a factor of three reduction in continuum signal to noise in the final co-adds, primarily due to the significant variations in instrumental, sky (e.g. twilight and moon illumination) and thermal (especially in K-band) background between object and adjacent sky frames. Instrumental variations include a readout channel dependent effect, which can vary frame to frame. To account for this effect, we derive and subtract a background value for each of the readout channels of the detectors.

3.2. *Astrometric Registration, Improved Background Subtraction and Generation of Combined Cubes*

After the reconstruction of individual frames, *Partial* combined cubes, defined to be the co-add of the data taken for a given galaxy within a given observing setup (commonly one per observing run), are generated assuming astrometric shifts between frames equal to the average of the measured shifts for the three stars included in the same setup (this accounts for the telescope dithering and the gradual drift of the KMOS arm positions).

We also generate 100 bootstrap cubes obtained by randomly resampling the input frames for each partial combine. We use these cubes for the propagation of uncertainties. In this work, we make use of a modified combined noise cube with the aim to obtain a robust estimate of the spectral uncertainty close to the edges of the cubes where few exposures are available (given that SPARK estimates variance from the distribution of values in each exposure). We derive a single variance spectrum per cube using the SPARK variance estimate in spaxels to which at least 75% of the total number of exposures have contributed. We then scale this spectrum by the exposure time of each pixel in the cube.

To achieve the best signal to noise ratio and image quality for our data in the final cubes we further process the individual frames to obtain a flat background and an accurate registration of the astrometry between frames observed in different runs. To do this we generate images of each galaxy by collapsing the KMOS partial combine datacubes along the wavelength axis. The galaxy continuum is well detected for most sources brighter than our $Ks = 23$ magnitude limit, with an increasing fraction of non-detections in continuum close to this limit ($\sim 11\%$ in the range $Ks = 22.5 - 23$).

At this stage, the partial combine cubes retain a residual, negative background caused by the overestimation of background levels in individual frames due to the contribution of the source. Its magnitude in bright sources is $\lesssim 10\%$ of the variation in background level between exposures and decreases in fainter sources, but it is systematic and limits the depth of our final mosaics. Thus, we derive an additive correction to the background as described below.

We first convolve the HST image, selected in the nearest available band (WCF3 F125W for KMOS YJ, WFC3 F160W for KMOS H and K) with a multi Gaussian kernel to optimally convolve the HST PSF to that of our KMOS PSF image for that galaxy. Each model solution is defined by an astrometric offset, a normalising flux scale factor and an additive background correction per readout channel which contributes in the partially combined datacube. Each model image is generated by projecting the convolved HST image onto the KMOS pixel grid and cropping to the KMOS field of view, and then adding the background correction image. We use the MPFIT non-linear least squares fitting algorithm to find the minimum chi-squared solution (Markwardt 2009)[17]. To ensure we do not get stuck in a local minimum, we iterate over the initial guess for the astrometric centroid on a grid of 1 pixel resolution, allowing centroids within $\pm 30\%$ of the FOV from the image centre, selecting the solution which gives us the global minimum chi-squared. The full procedure is repeated for each bootstrap cube (except the initial guess for the astrometric centroid is now fixed) to help evaluate errors and degeneracy in the astrometric registration.

Of 166 objects with multiple setups, the median residual shift is ~ 1.33 KMOS pixels ($\sim 0.27''$) with $\sim 27\%$ of shifts above 2 KMOS pixels ($0.4''$), ranging as high as 4.35 pixels ($0.87''$).[18] Not accounting for such shifts artificially blurs the galaxy by an average of $\sim$2 kpc and up to $\sim$7 kpc. These shifts are caused by the variations in the calibration parameters of individual KMOS arms, which are periodically tweaked by the observatory to ensure that the arm positioning remains within specifications. Fits to the individual partial combines are visually inspected and a new list of astrometric shifts is derived by combining the frame to frame shifts measured using PSF stars and the setup to setup shifts from the fits of partial combines. We also subtract the best-fit background image from each individual exposure contributing to a given partial combine cube.

With the updated list of astrometric shifts, we combine all frames contributing to a single object and we re-generate the bootstrap cubes. This produces our final *total* combined datacubes. At this stage we also derive the instrumental resolution for each cube and its associated PSF image. For a detailed description of these procedures we refer the reader to W19. No correction is applied during the fit of partial combines to the absolute astrometry. This is done by fitting the total combines in order to have the deepest KMOS images register onto the HST astrometry. This last fit does not include a background level as the background has already been flattened during the previous step.

Each astrometric solution is now visibly inspected by looking at the object centroid in the collapsed KMOS image, and in the model HST image. In 615 of 645 cases the automated solution is good, as in the example case shown in Figure 1. These imply a median shift of ~ 1 KMOS pixel ($0.2''$) with a tail extending to > 5 pixels ($> 1''$) and a median bootstrap error of ~ 0.1pixel, with errors up to ~ 1 pixel. This is consistent with the shifts computed for the same object observed in multiple setups and with the expected positioning accuracy of the KMOS arms. In 26 cases we apply a manual shift, of which for 15 it was necessary to inspect also the Hα image. We used this image to confirm the low signal to noise continuum centre finding consistency with the Hα image in all cases. Only four targets are not visible in continuum or Hα,

[17] https://www.physics.wisc.edu/~craigm/idl/fitting.html

[18] W19 reports a lower fraction of large shifts because in that paper we divided the list of exposures into smaller units with smaller shifts for the final data release.

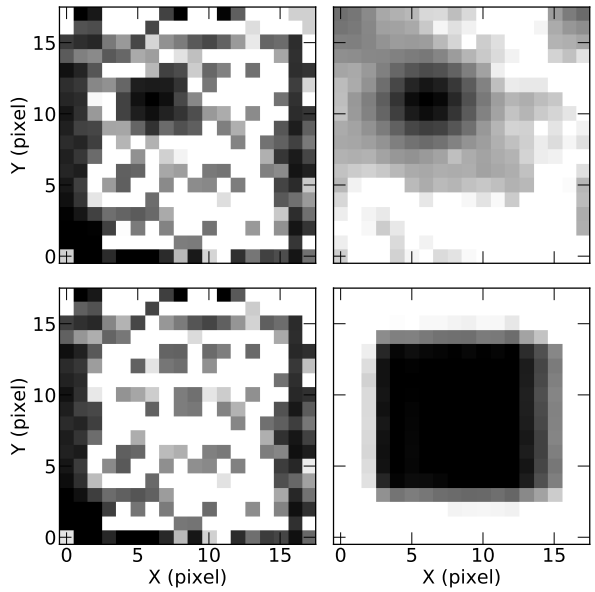

Figure 1. Example of astrometric registration fitting procedure. The collapsed KMOS continuum image (top-left) is fit to the PSF-convolved and resampled CANDELS image in the nearest band, including a shift (top-right), leaving the residual image (bottom-left). Fitting weights are applied (bottom-right) which down-weight the outer part of the image (subject to cosmetic effects and lower total exposure). For this example case (COS4_12148) a large shift of 2.5 pixels each of X and Y is required.

for these no astrometric correction is applied. Manual astrometric solutions are usually accurate within a pixel, with the exception of some low S/N continuum or Hα-based centroids which can be less accurate (up to ~ 2 pixels).

The astrometric correction derived above is applied, registering datacubes and bootstrap cubes to the HST astrometry. These astrometrically and background corrected cubes are considered our final datacube products.

4. GENERATION OF MAPS AND PROFILES

4.1. *Emission Line Measurement*

To fit the Hα+[NII] emission line complex we utilize our versatile IDL-based emission-line fitting software KUBEVIZ[19]. (see e.g. Fumagalli et al. 2014; Fossati et al. 2016). KUBEVIZ can be operated in interactive or batch modes, and provides the user with full access to the options provided by MPFIT which fits the continuum and emission lines. Gaussian fits to emission lines automatically account for the (known) spectral resolution of the instrument as a function of wavelength.

We derived accurate maps of emission line flux down to low surface brightness levels, as well as velocity maps and masks of good kinematic fits as described below.

4.1.1. *Kinematic Fits*

Our first fit is mostly aimed at generating velocity and dispersion maps. To improve the S/N per pixel, the flux, noise and bootstrap cubes are median smoothed along spatial axes with a top-hat smoothing kernel of 3×3 spaxels. We fit the spectral continuum underlying the Hα + [NII] emission line complex, assuming a constant value, independently computed for each spaxel, $C_{x,y}$. This is the inverse-variance weighted average value within spectral continuum windows defined to either side of the Hα line, corresponding to between 2000 km s^{-1} and 5000 km s^{-1} in rest-frame velocity offset (thus excluding [NII] and [SII] lines). The spectral region from 12680-12710Å containing the strongest part of the atmospheric O2 feature, and regions within 10Å of either end of the spectrum are excluded. We generate continuum-subtracted cubes $CS_{x,y,\lambda}$ by subtracting the continuum for all spaxels from the flux cube, $F_{x,y,\lambda}$, in symbols:

$$CS_{x,y,\lambda} = F_{x,y,\lambda} - C_{x,y}. \quad (1)$$

We simultaneously derive kinematic and flux information for the Hα, $[NII]\lambda6583$ and $[NII]\lambda6548$ emission lines by fitting the inverse-variance weighted continuum-subtracted spectra for each spaxel. We fit a single Gaussian line profile for each emission line which accounts for the redshifting and instrumental line broadening of the specific KMOS observation, returning the rest-frame velocity and intrinsic dispersion of the ionized gas. Since, for this step, we are interested in robustly detected emission lines, these fits are constrained such that lines have a minimum of zero flux. Multiple lines all share a single velocity and dispersion, and the ratio of flux in the two [NII] lines is fixed to the value from atomic physics (3.071, Storey & Zeippen 2000). As a result, output 2-D maps are generated for each fit parameter (line flux, velocity, dispersion).

The full continuum and emission line fitting process is repeated for each bootstrap cube, generating 100 bootstrap realisations of the fitting parameters. These are used to generate images where each spaxel represents the probability of non-zero Hα line flux $P_{f_{H\alpha}>0}$ and positive non-zero dispersion $P_{\sigma>0}$. $P_{f_{H\alpha}>0}$ represents a detection significance of the flux per spaxel, and $P_{\sigma>0}$ that the emission line is significantly resolved. High values $P_{\sigma>0} \gtrsim 0.9$ provide a good indication that MPFIT has picked up a real feature in the spectrum rather than a noise or skyline residual spike, and correlates well with regions where the velocity map is relatively smooth. Intrinsic velocity dispersions of $\sigma \gtrsim 25$ km s^{-1} are usually well resolved.

4.1.2. *Masking*

We then generate an automated spaxel mask to identify spaxels with trustworthy kinematic fits. Within this mask, a good (unmasked) spaxel must meet the following conditions:

$$\begin{array}{llll} (f_{H\alpha} > 0.) & \text{and} & (0 < \sigma \leq \sigma_{max}) & \text{and} \\ (P_{f_{H\alpha}>0} \geq 0.95) & \text{and} & (P_{\sigma>0} \geq 0.9) & \end{array} \quad (2)$$

where we set $\sigma_{max} = 250$ km s^{-1} to exclude broad line features, given that our primary goal at this stage is to define the velocity map. This mask is applied to the velocity map of example galaxy U4_25642 in the left-hand panel of Figure 2.

We then apply some further steps designed to throw out potential outlier spaxels in the velocity map. The sigma-clipped mean and rms velocities are computed,

[19] KUBEVIZ is made publicly available at https://github.com/matteofox/kubeviz and http://www.mpe.mpg.de/~dwilman/kubeviz and is easily adaptable to new instruments.

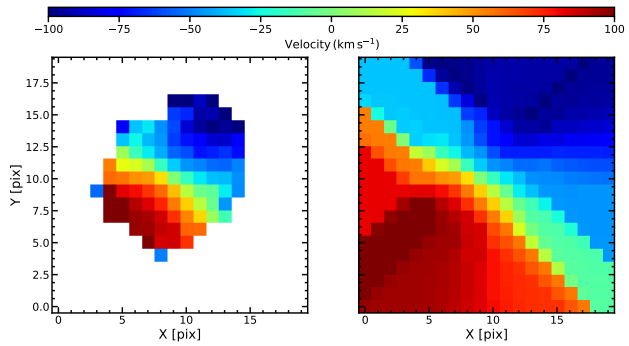

Figure 2. Example masked velocity field (left) and grown velocity map (right) for galaxy U4_25642. Blank pixels in the left hand image are masked, using the pre-sigma clipping mask discussed in the text. Additional automated sigma-clipping and (in some cases) additional manual editing of the mask are then applied, followed by smoothing and growth by extrapolation of the masked velocity map to generate the grown velocity map as described in the text.

and any spaxel with velocity outside the range mean $\pm$ $3\times$rms is thrown out. Isolated unmasked spaxels are removed and the remaining are smoothed with a 3×3 top-hat filter. This leaves us with a conservative mask and a smooth velocity map. While conservative, our maps are consistent with those presented in other KMOS^{3D} papers focused on galaxy kinematics (see e.g. Wisnioski et al. 2015).

Galaxies with <3 valid spaxels are dropped, as are poor fits established by inspecting objects with <10 valid spaxels. This relatively small minimum number of spaxels is sufficient to establish a zero-point and lack of chaotic variation in the velocity maps of compact galaxies which is sufficient for our purpose. This leaves 462 galaxies. All velocity maps are visually inspected, resulting in the removal of a further seven cases (leaving 455 galaxies) and the manual correction of 117 masks. These fix cases in which the rotation curve gets truncated by the sigma-clipping procedure, or there are systematic fits to sky features which are usually spatially offset from the galaxy, and are not sigma-clipped.

We then extrapolate the rest-frame velocity map to the edges of the KMOS field of view to generate a *grown velocity map*, $dv_{rest}(x,y)$. This involves setting the velocity of masked spaxels to the average value of their neighbours, starting with those with unmasked neighbours and iterating up until the point that the whole area is filled. While this extrapolation cannot pick up changes in the rotation curve in the outer, low surface brightness parts of the galaxy, it involves minimal assumptions. This procedure is repeated for each bootstrap iteration independently. The right-hand panel of Figure 2 shows the resultant grown velocity map for U4_25642.

4.1.3. *Deep emission line flux maps*

To derive our final Hα flux maps we reapply continuum fitting and subtraction, this time to the *unsmoothed* cubes. Then we integrate the flux within each spaxel of the continuum-subtracted cube, centred at the wavelength specified for Hα, assuming the "grown" velocity map. In the observed-frame this is $\lambda_{cen}(x,y) = \lambda_{\rm H\alpha}.(1+dv_{rest}(x,y)/c)\times(1+z)$ with a window width of $\pm200\times(1+z)\,{\rm km\,s^{-1}}$. This window is sufficiently wide to encompass offsets from the true velocity caused by the extrapolation process into the outer disk (see e.g. Lang et al. 2017), without losing too much flux in the wings of all but the broadest emission lines. A broader window would lead to reduced signal-to-noise. This narrow-band extraction generates a map of Hα flux down to regions of low signal-to-noise where parametric fitting fails or becomes unreliable. Our window-integrated Hα map is computed as:

$$\mathrm{f_{H\alpha,WIN}(x,y)} = \Delta\lambda\cdot\Sigma_{\lambda_{\rm upper}(x,y)}^{\lambda_{\rm lower}(x,y)}\mathrm{CS_{x,y,\lambda}} \qquad (3)$$

with the bounds in the sum given by $\lambda_{cen}(x,y)\pm(200\,{\rm km\,s^{-1}}/c)\times(1+z)$, and $\Delta\lambda$ being the spectral step (in Å) of the datacubes. This procedure is again repeated for each of the 100 bootstrap realizations.

Finally we correct these flux maps $\mathrm{f_{H\alpha,WIN}(x,y)}$ for flux lost outside the $\pm200\,{\rm km\,s^{-1}}$ window from the tails of broad lines. An alternate mask is used to define regions for which the velocity and dispersion from Gaussian fitting is usable for this purpose: this is equivalent to equation 2 but with a relaxed upper limit on dispersion σ: in this case $\sigma_{\rm max}=1000\,{\rm km\,s^{-1}}$ for $\mathrm{S/N_{H\alpha}}\geq4$ and $\sigma_{\rm max}=400\,{\rm km\,s^{-1}}$ for lower $\mathrm{S/N_{H\alpha}}<4$ (thresholds selected from visual inspection of fits to broad lines). Isolated, unmasked spaxels are thrown out, and manual edits made to our earlier masks are reapplied to this mask. The dispersion measured by the fit is used to compute the fraction of emission flux which falls outside our $\pm200\,{\rm km\,s^{-1}}$ window, and this correction is applied to the flux map:

$$\mathrm{f_{H\alpha,WINcor}(x,y)} = \mathrm{f_{H\alpha,WIN}(x,y)/c_{\sigma_{200}}} \qquad (4)$$

with $\mathrm{c_{\sigma_{200}}}$ the two-tailed cumulative distribution function for a Gaussian, evaluated at $\sigma_{200}=\sigma/200\,{\rm km\,s^{-1}}$. The correction is usually small except in regions containing very broad lines ($c_{\sigma_{200}}=0.955$, 0.576, 0.197 for velocity dispersions $\sigma=100\,{\rm km\,s^{-1}}$, $250\,{\rm km\,s^{-1}}$, $1000\,{\rm km\,s^{-1}}$ respectively). Outside the mask we do not have reliable data to make a correction. However, these regions usually correspond to the outer and low surface brightness parts of galaxies where the dispersions are typically low $\lesssim100\,{\rm km\,s^{-1}}$ Wisnioski et al. (2015) and so any correction would be very small.

This correction is also applied to the bootstrap realizations, and we consider $\mathrm{f_{H\alpha,WINcor}(x,y)}$ our best estimate of the flux map for the Hα emission line, from now on simply known as the Hα flux map or image.

4.2. *Image Fitting in 2D*

We now model the radial surface brightness profiles by fitting the images of our galaxies in 2D using the Levenburg-Marquardt solver from the image fitting code IMFIT[20] (Erwin 2015). Our goal is to quantify the distribution of continuum flux (in particular the F160W band tracing older stars), and Hα flux (tracing ongoing star-formation) obtained with the spectral windows method defined above. We fit continuum profiles with a Sersic profile (Sersic 1968) and Hα profiles with a pure exponential, motivated by the results of Nelson et al. (2016a). Despite radial and / or azimuthal variations from a pure exponential profile, the best-fit solution will account for the mean surface brightness at fixed

[20] http://www.mpe.mpg.de/ erwin/code/imfit/

radius, and as such provides a measure of the average star-formation at that radius, smoothing out temporal fluctuations due to bursty star-formation on local scales and the short-lived nature of the Hα emission. This is demonstrated by the accuracy of the exponential fit viewed as 1D azimuthally-averaged radial profiles.

We fit Sersic models convolved to the HST PSF, as derived by the 3D-HST team (Skelton et al. 2014), to postage stamps of each galaxy in F160W and F125W bands Fitting F160W data, the centroid, ellipticity and position angle are left free in addition to the effective (= half-light) semi-major axis radius r_e, Sersic index $n_{\rm Sersic}$ and normalizing surface brightness. Initial guesses for fit parameters are taken from the fits of van der Wel et al. (2014b, , hereafter vdW14) using the GALFIT-software (Peng et al. 2010)[21]. To estimate initial parameters for galaxies which were not fit by GALFIT (flags of ≥ 2 in the vdW14 catalog), we use the SExtractor parameters from Skelton et al. (2014) and empirical relations between SExtractor and GALFIT parameters for size, axis ratio ($q = 1-\epsilon$ where ϵ is the ellipticity) and position angle. This includes empirical fits for size and axis ratio to those objects which were fit well by GALFIT, using the SExtractor major and minor axis size parameters A_IMAGE and B_IMAGE:

$$\begin{aligned} r_e &= 1.25 \times \sqrt{\text{A\_IMAGE}^2 - 0.15^2} \\ q &= \sqrt{B\_IMAGE^2 - 0.15^2}/\sqrt{A\_IMAGE^2 - 0.15^2} \end{aligned} \quad (5)$$

To avoid biased fits due to neighbouring galaxies, we simultaneously fit all neighbouring galaxies within 5″ and less than 3.5 magnitudes fainter than the primary source in both bands (F160W and F125W), or within 2″ and less than 5 magnitudes fainter. The left-hand panel of Figure 3 demonstrates the good agreement of effective radii fit using IMFIT and GALFIT. The few outliers mainly move along the degeneracy between $n_{\rm Sersic}$ and r_e and tend to include multiple simultaneously fit objects of similar magnitude.

We also fit the KMOS continuum image and bootstrap realizations (a resistant weighted mean along the wavelength axis as described in Section 3.2) with the same set of constraints, resulting in similar fits, though the lower signal to noise leads to a larger scatter about the 1:1 relation (right-hand panel of Figure 3).

Finally we fit the Hα flux image (precisely, $f_{\rm H\alpha,WINcor}(x,y)$) and bootstrap realizations. The Hα disk is modelled with a simple exponential profile convolved with the KMOS PSF and with the KMOS pixel size and field of view. We only fit data from spaxels with at least 20% of the nominal number of exposures for each object.[22]. Unlike continuum fits, we only fit the primary galaxy (as in all but a few cases the redshift of any photometric neighbours puts any emission line outside our windows for Hα or continuum). The centroid, ellipticity and position angle are fixed to those measured at HST native resolution in F160W band to ensure that we are geometrically tracing the same disk in star-formation as we see in stars. The half-light radius starting guess is fixed to that of the stars: we confirm that this has no influence on our results by re-fitting each source (excluding the bootstraps) with the slower differential evolution solver method which does not require initial estimates for the parameters. For all galaxies in our analysis (see Section 5.1) the resultant sizes are identical. A minority of galaxies do not host such star-forming disks but do still host Hα emission tracing some other component (e.g. outflows) which is not only physically disassociated to the disk , but does not share its inclination and geometry. Cases which are not well modelled by the exponential disk model are flagged as described in Section 5.1. We further investigate the impact of our assumption of an exponential profile for the Hα emission by fitting Sersic models to these images. We find that, for most of the sources in our analysis, the best fit Sersic index is close to unity and the effective radii are consistent with those from the exponential fits. Quantitatively we find consistency between r_e from Sersic and exponential fits within 1, 2, and 3σ for 65%, 75%, and 86% of the galaxies in our sample, respectively. We also find that the trends presented in Section 6 are unchanged within the uncertainties. However, a substantial number of Hα images whose Sersic fits hit the fitting limits for the Sersic index, leading to more discrepant values for r_e when compared to the exponential fits. For these reasons, in this work, we use the results of the exponential fits to the Hα images.

Appendix A describes how we test and derive final errors on size measurements, concluding that not only are the continuum sizes consistent with those from HST as shown in Figure 3 but that deviations are, statistically, very consistent with our errors, and that the accuracy of our PSF model is not the dominant source of error.

4.3. *Major Axis Radial Profiles*

For our current purposes we are not interested in azimuthal variations. Therefore to establish that the radial flux profiles are indeed well characterized by the model and fit, we also extract one-dimensional radial surface brightness profiles in elliptical annuli, aligned to the galaxy's best fit ellipticity and position angle. In practice these are computed by embedding the images in a larger grid, weighting the individual image pixels by their effective contribution per radial bin, and then integrating the flux within differential elliptical bins corresponding to a given major-axis-equivalent radius. Equivalent profiles generated from each bootstrap image provide estimates of the error on the profile. We also generate profiles for the best IMFIT fit model profiles in the same way – the projection of the model image onto elliptical radial apertures, and of the PSF (placed at the centroid of the galaxy). This enforces the same pixelization as exists in the data itself for direct comparison. In Appendix B we show a gallery of Hα profiles spanning a range of size, redshift and observed surface brightness, to highlight the quality of the data and of the fitting procedure.

5. SAMPLE

5.1. *Flagging*

[21] We intialize the centroids to the best fit ones from GALFIT, not SExtractor as published, private communication with A. Van der Wel.

[22] For four objects in our sample, this threshold would result in spaxels with less than 5 individual exposures, in this case we used the latter value to define the spaxels to be fit.

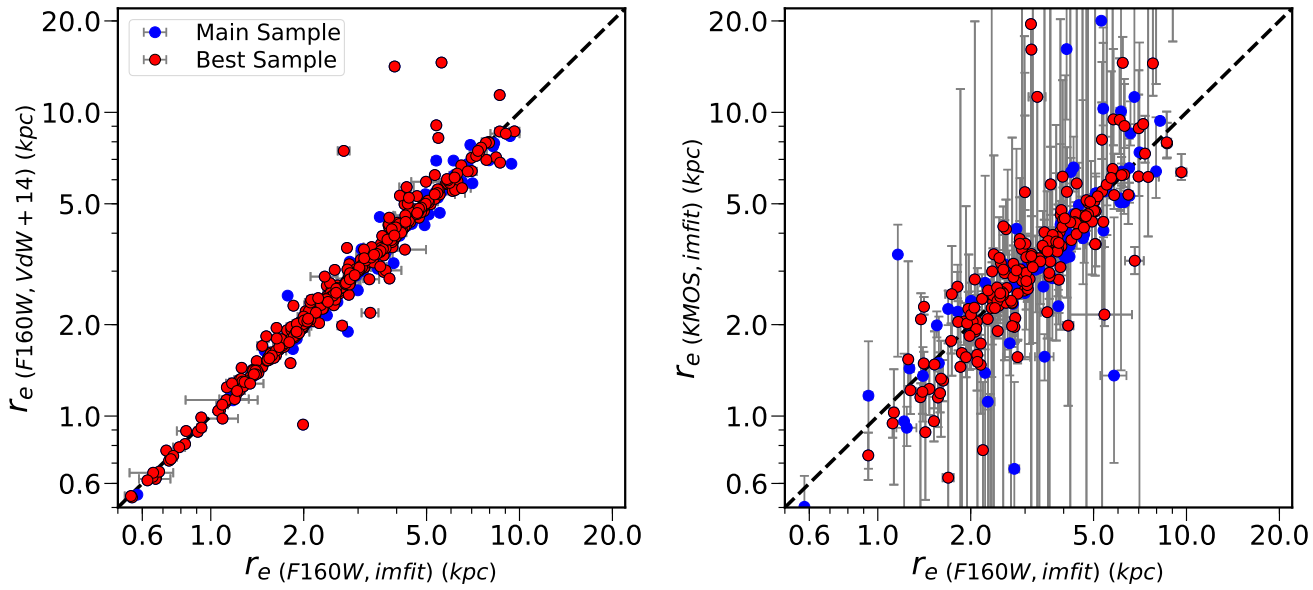

Figure 3. Measurement of intrinsic half-light size for valid fits (see text). Left: IMFIT-based fits to F160W-band CANDELS data at native HST resolution (this paper) compared to GALFIT fits from vdW14. Medians are within 0.2% for main and best samples, and 68, 95% of galaxies within $^{+3}_{-5}$%, ±21% respectively. Right: IMFIT fits at full HST resolution vs those from the collapsed KMOS continuum (with bootstrap errors, see Section A. Fits are remarkably consistent: Medians are within 1%, 68% of galaxies are within ±23%, and outlying points tend to have large errorbars.

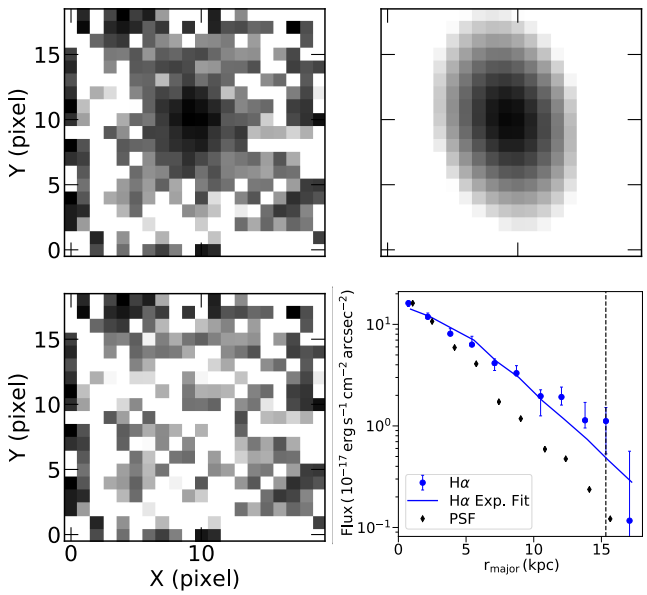

Figure 4. Example IMFIT fit to the data for galaxy GS3_11606. Top-left: log-scaled Hα image; top-right: Best fit model exponential galaxy convolved with PSF, from IMFIT (log-scaled); Bottom-left: Residual image (linear scaling); Bottom-right: Log-scaled radial profile, extracted using elliptical apertures from both data (blue points with $1-\sigma$ bootstrap errors) and best fit model (blue solid line) images. For comparison, the PSF image is also extracted in the same apertures (black diamonds). The residual image and 1D profile demonstrate a good fit for this galaxy, with a best fit size of $r_e = 3.74^{+0.6}_{-0.45}$ kpc. The vertical dashed line indicates the radius where the major axis first crosses the edge of the KMOS field of view.

Our analysis requires size estimates which accurately reflect the true profiles of continuum and Hα. Starting with our astrometrically calibrated, Hα-detected and masked sample with valid velocity grown maps (457 galaxies), we need to weed out objects with strong skyline contamination or poorly fit continuum / Hα profiles. We do this via a series of steps during which two authors (MF and DJW) independently visually inspected the data, removing objects not satisfying a series of requirements.

This results into a sample including all the objects for the analysis of the Hα and F160W sizes (the Hα sample hereafter), which we further split into a MAIN and a BEST sample, where the BEST sample includes only the best IMFIT fits and sky subtraction (for Hα) while the MAIN samples include all reasonable fits.

In detail, we first we inspected the data for atmospheric skyline residual contamination which is evaluated by simultaneously inspecting the inverse-variance weighted summed spectrum within the mask of good Gaussian fits, the variance spectrum, and the inverse-variance weighted summed spectrum from outside the mask. The comparison of spectra inside and outside the mask serves to establish which spectral features are associated to the galaxy spectrum and which are spurious features commonly associated to high variance residuals from sky-subtraction. 83 of 457 galaxies have strong skyline contamination and will be excluded from further analysis while 101 have a weaker contamination (skyline residuals are sub-dominant compared to the underlying Hα emission, or lie just outside the Hα wavelength range). The latter are included in the analysis as part of the Hα MAIN sample, but we examine their influence on our results by excluding them from the Hα BEST sample.

We also exclude 22 of the remaining galaxies due to close pairs for which the paired galaxy also appears in the Hα image, two galaxies with PSF axis ratios > 1.5

and six galaxies for which the apparent, measured Hα flux is incoherently spread across the FOV.

In general, our fits are deemed to be good if: a) the magnitude of fractional residuals and χ^2 in the image plane is visually defined to be small; b) the 1-D extracted profiles from data and best fit are visually in close agreement (and, generally within the errorbars in radial bins)[23]; c) IMFIT converged on a best-fit which did not hit the parameters limits. For Sersic fits to the continuum, the parameters are limited to the range: $0.2 < \mathrm{n_{Sersic}} < 8.0$, surface brightness $\mathrm{I(r_e)} > 0$, $0.01\,\mathrm{kpc} < \mathrm{r_e} < 99\,\mathrm{kpc}$ and for exponential fits to Hα, central surface brightness $0 < \mathrm{I_0} < 10.\mathrm{I_{peak}}$ where I_{peak} is the maximum surface brightness per pixel, and $0.01\,\mathrm{kpc} < \mathrm{r_e} < 99\,\mathrm{kpc}$. 399 of 457 galaxies meet these criteria, of which 207 fits are excellent.

At native CANDELS resolution in F160W, 559 of 645 galaxies are well fit with a single Sersic profile. We also require best fit CANDELS F160W ellipticities $\epsilon < 0.7$ (which corresponds to an inclination of $i \gtrsim 72.5$ in an infinitely thin disk) because for the edge-on cases the intrinsic disk thickness cannot be ignored.

Merging all these criteria, our final Hα MAIN sample contains 281 galaxies, with 89 in the Hα BEST sample. For the remainder of the paper we will discuss the results derived for the Hα MAIN sample only, having tested that there are no qualitative changes if we restrict to the Hα BEST sample.

Of the final Hα MAIN (BEST) galaxy sample, 42 (11) have clear broad lines, and 38 (13) have known AGN. We do not remove these from the samples as these galaxies have been screened for a good fit exponential profile, suggesting that the outflow / AGN does not dominate the profile. Results are examined with and without these objects, with no notable difference to our conclusions.

The samples for comparison of CANDELS F160W and KMOS continuum sizes are slightly different, requiring good (excellent) fits in both continuum bands and ellipticities $\epsilon < 0.7$. This results in sample sizes of 288 and 193 for the continuum MAIN and continuum BEST samples respectively. Galaxy sizes and errors for the Hα MAIN sample are provided in Appendix C for the on-line version of the article.

5.2. *Sample Bias*

Figure 5 examines whether any bias might be introduced through galaxies remaining undetected or unmapped in Hα or otherwise not included in the Hα MAIN or BEST samples. The upper panel shows the difference between a galaxy SFR and the main-sequence SFR of a galaxy at the same mass and redshift using the prescription derived by Whitaker et al. (2014). We show only galaxies observed by KMOS^{3D}: see Wisnioski et al. (2015), Wuyts et al. (2016), and W19 for the impact of our Ks-band selection in this plane. All 645 target KMOS^{3D} galaxies are shown in Figure 5. The middle panel shows the location of the same galaxies in the F160W half-light size - stellar mass plane. The lower panel shows the galaxies in the "UVJ" (U − V vs V − J) color-color plane (Williams et al. 2009), which separates

[23] Note: not all radial bins have to be consistent with the fit: our flag represents an *average* and is meant to indicate if the size measurement is likely to be biased.

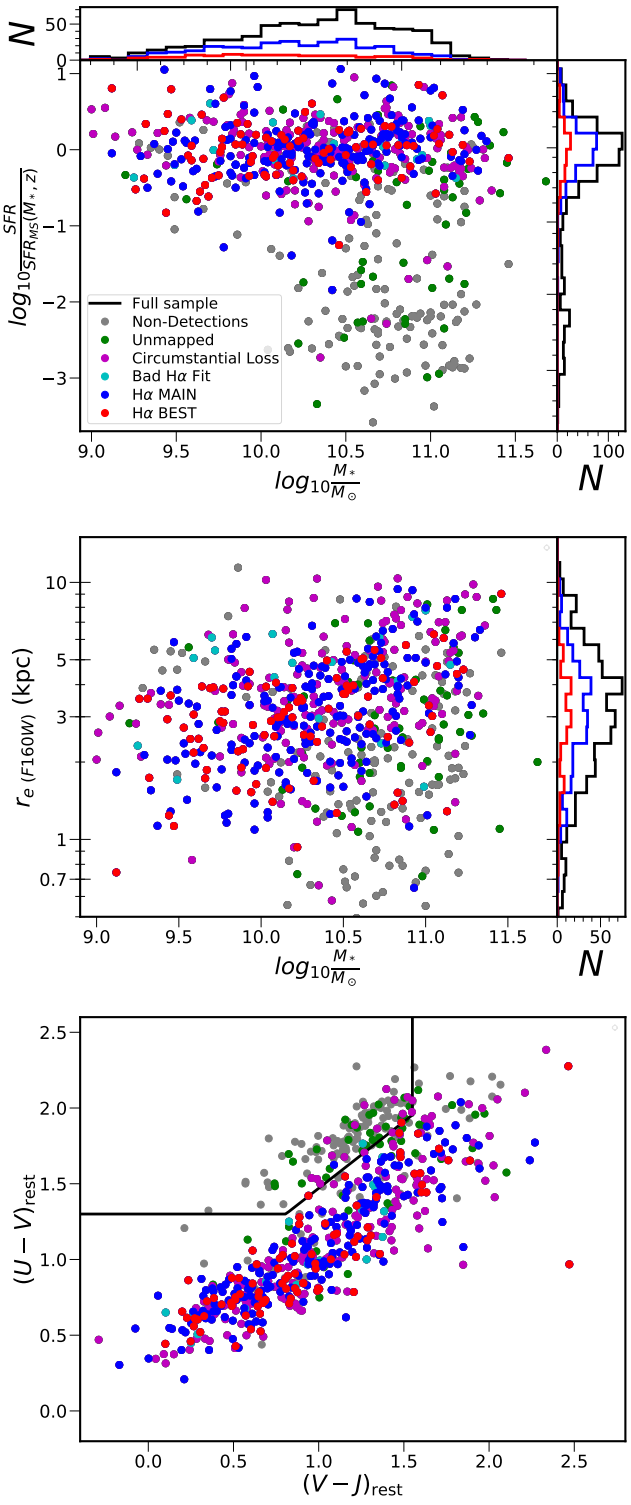

Figure 5. Upper panel: Offset in SFR of each KMOS^{3D} galaxy from the main sequence at its stellar mass and redshift, as defined by Whitaker et al. (2014); middle panel: continuum (F160W) size versus stellar mass; and lower panel: U − V vs V − J colour-colour space (passive galaxies are to the top-right of the black demarcation line). The histograms show the marginalized distributions for the full, Hα BEST and Hα MAIN samples in stellar mass, SFR, and galaxy size. Galaxies in the Hα BEST and Hα MAIN samples occupy the whole main sequence, falling off to low SFR and into the passive region of the colour-colour space. These samples are therefore representative of normal main sequence galaxies, with no significant detection bias.

passive galaxies from star-forming galaxies (at the black demarcation line). Using two colors it is possible to disentangle passive galaxies (top left) from optically red, dusty star-forming galaxies (top right).

Figure 5 shows that the fraction of galaxies with detected Hα is high for main sequence galaxies, then drops rapidly to low SFR and redder colors. Galaxies designated "unmapped" in Figure 5 can have either low signal to noise ratio or chaotic kinematics / dominant broad line components, and it is impossible to trace a dominant star-forming disk-like component. Combining non-detections and unmapped galaxies accounts for 83% of UVJ passive galaxies and 98% of galaxies more than 1.0 dex below the main sequence, but only 14% of UVJ star-forming galaxies and 11% of galaxies less than 0.3 dex below the main sequence. Of this, the unmapped population contributes an increasing fraction at high mass, reaching $\sim 20\%$ for $\log_{10}(M_*/\mathrm{M}_\odot) > 10.9$ galaxies within 1 dex of the main sequence. These very massive objects are more difficult to map in Hα due to their lower specific star formation rates and higher dust extinctions, which in turn make their redshift determinations more uncertain. However, the number of these objects is relatively low and we found no significant difference in the distributions of size and offset from the MS for the Hα MAIN sample if we split above and below $\log_{10}(M_*/\mathrm{M}_\odot) = 10.5$. The H$\alpha$ MAIN sample probes well into the dusty star-forming region of the UVJ diagram, which is a key feature of the KMOS^{3D} survey design (see Wisnioski et al. 2015, 2019) that helps in reducing selection biases for our sample. Along the main sequence, most galaxies which are not in the Hα MAIN sample are dropped for circumstantial reasons which does not introduce any selection bias (magenta points), i.e. mostly due to significant sky line residuals or high ellipticity. The cyan points denote the few galaxies with clean, mappable emission line signal for which the exponential fit to Hα emission was flagged as bad. There are 18 such objects of which the majority display Hα emission offset from the continuum and some are clear mergers. These galaxies tend to have large continuum sizes for their stellar mass (lower panel), but given their small number and, for some of them, uncertain continuum sizes, we consider there to be no notable bias against normal disk-like extended star-forming disks in our sample. Finally, we note that there is no notable difference in the properties of Hα MAIN and Hα BEST galaxies supporting our decision to focus on the Hα MAIN sample.

6. RESULTS

6.1. Hα *size correlations with continuum size and stellar mass*

Armed with accurate galaxy half-light (size) measurements in continuum (tracing stars) and in Hα (tracing star-formation), we now examine how the extent of star-forming gas relates to other known galaxy properties. In particular, we are interested in how closely the distribution of new stars, as traced by Hα, follows the distribution of old stars. Before answering this question we turn our attention to the best tracer for the size of old stars. Kelvin et al. (2012), and vdW14 showed that the star-forming galaxies have negative color gradients,

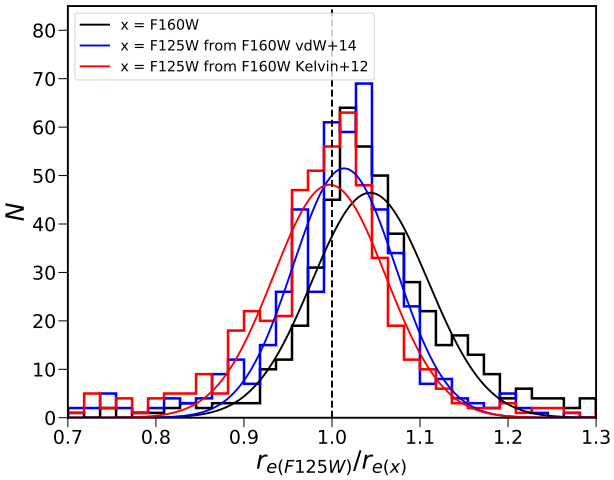

Figure 6. Histograms of the ratio of the best fit half-light size in the F125W band to that in the F160W band for galaxies in the CONTINUUM MAIN sample, and a Gaussian best fit (black lines). The blue and red lines show the ratio with observed F160W sizes corrected to F125W with the fitting functions of vdW14, and Kelvin et al. (2012), respectively. The black dashed line marks where the size ratio is unity.

implying that their size is smaller at longer rest-frame wavelengths. This is shown in the black histogram of Figure 6, where we plot the ratio of sizes in F125W to F160W. The center of the Gaussian fit assumes a value 1.042 for the size ratio. Kelvin et al. (2012), and vdW14 provided fitting functions for the wavelength dependence of the observed size, which we applied to our observed F160W sizes to correct them to F125W. We note that the Kelvin et al. (2012) correction is only a function of observed wavelength, while the vdW14 correction depends also on the galaxy stellar mass. The blue and red histograms and Gaussian fits show that these corrected sizes match the observed F125W sizes much better than the uncorrected data with average ratios of 1.013 and 0.997 for vdW14 and Kelvin et al. (2012) respectively. Due to the simpler nature of the correction proposed by Kelvin et al. (2012), and its excellent accuracy in correcting the sizes in our sample, we use this fitting function to correct the observed F160W sizes to rest-frame 6500Å. This rest-frame wavelength has multiple advantages: first and foremost it is close to the rest-frame wavelength probed by F160W in the center of our redshift range, and therefore a roughly equal number of galaxies are corrected to a shorter and longer wavelength. Moreover, it is close to the rest-frame wavelength of the Hα emission, mimicking the observing strategy of narrow band surveys in the local Universe (where the continuum size is evaluated from a filter close in wavelength to the narrow band filter used for the Hα observations, as done by e.g. Fossati et al. 2013; Boselli et al. 2015). We add scatter to the correction applied to individual galaxies by randomly sampling a Gaussian function with σ equal to the standard deviation of the Gaussian fit shown in Figure 6. Hereafter we will use this corrected continuum size as a tracer for the size of the old stars and we label it $r_{e(\mathrm{r6500})}$, unless otherwise noted.

At high redshift, the high gas masses, densities and

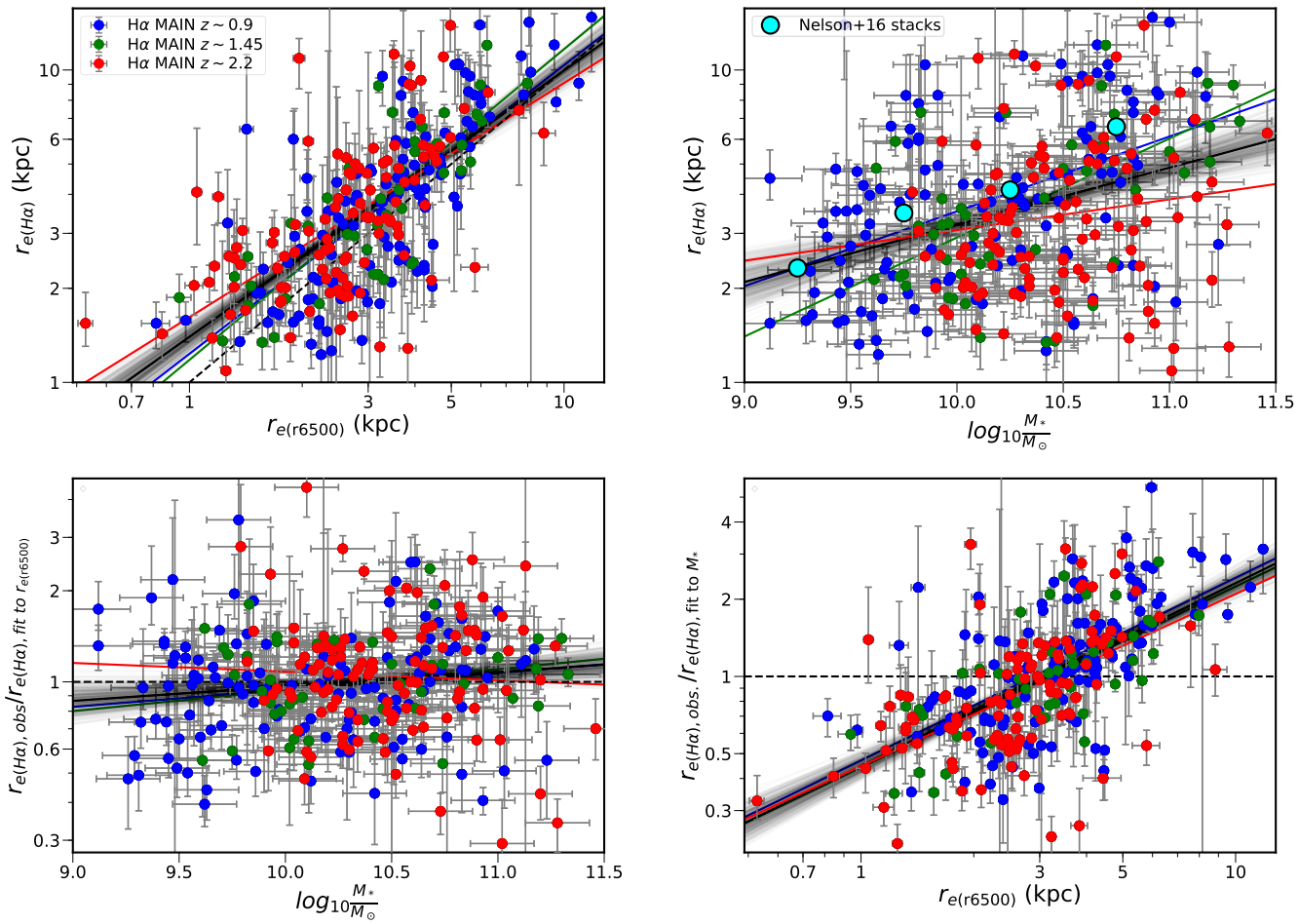

Figure 7. Top panels: Hα galaxy size plotted against: (left panel) galaxy size measured at 6500Å rest-frame band (from F160W data corrected with the Kelvin et al. (2012) function) and (right panel) galaxy stellar mass. The best fit and sample fits from MCMC are shown with the black solid line and fainter grey lines. Galaxies are divided into three redshift bins (corresponding to the KMOS band for Hα observation) with data points and fits to each redshift bin shown with different colours. Points from the stacked, circularized Hα size measurements of Nelson et al. (2016a), assuming an average ellipticity of $\epsilon = 0.4$, are shown in bins of stellar mass. Bottom panels: Residual Hα size after subtraction of the best fit relation above, plotted against the other parameter. The dashed black horizontal line shows the level at zero residuals. The Hα size of a galaxy is more tightly correlated with its continuum size than with its stellar mass.

accretion rates of KMOS^{3D} galaxies means that their star-forming gas is mostly molecular. Well-defined global galaxy relationships such as that between total star-formation and stellar mass (the star-forming main sequence) exist primarily because total star formation rates, to first order, smoothly track accretion rates, which themselves depend mainly upon the global halo potential and growth (e.g. Bouché et al. 2010; Lilly et al. 2013). It remains unclear to what extent a strong evolution in mass and mass growth should be reflected in changes in galaxy size and size growth. Therefore we begin by asking whether the Hα size of galaxies is better correlated with stellar size or total stellar mass.

Figure 7 conclusively answers this question. In the upper panels, we plot the Hα size of Hα MAIN sample against continuum size (left panel) and stellar mass (right panel). The positive correlation between Hα and continuum size is strong and tight, a positive correlation exists also between Hα size and stellar mass, but with much larger scatter.

We fit these relations using the *linmix* package for python[24] which follows the Bayesian framework described by Kelly (2007) and encorporates measurement errors on x- and y- axes as well as an additional component of intrinsic scatter into the fit. This code makes use of Monte-Carlo Markov Chains (MCMC) to fit a linear relation (in this case in the log-log plane and so corresponding to a power law relation between linear quantities). A random uncertainty of 0.15 dex in $\log_{10}(M_*/\mathrm{M}_\odot)$ is included in the analysis, consistently with vdW14.

In the size-size plane, we find a mildly sub-linear best fit relation with a slope of 0.85 ± 0.05 and intrinsic scatter of $43\pm3\%$ (0.15 dex) at fixed continuum size, significantly smaller than that of continuum size versus stellar mass (56%, or 0.19 dex vdW14). This is shown by the black solid line in Figure 7, while the grey shaded area shows a wider range of draws from the posterior. The correlation with mass has a slope of 0.18 ± 0.03 and intrinsic scatter of $68\pm4\%$, and is roughly consistent with the stacked Hα size measurements of Nelson et al. (2016a) who provide

[24] https://github.com/jmeyers314/linmix

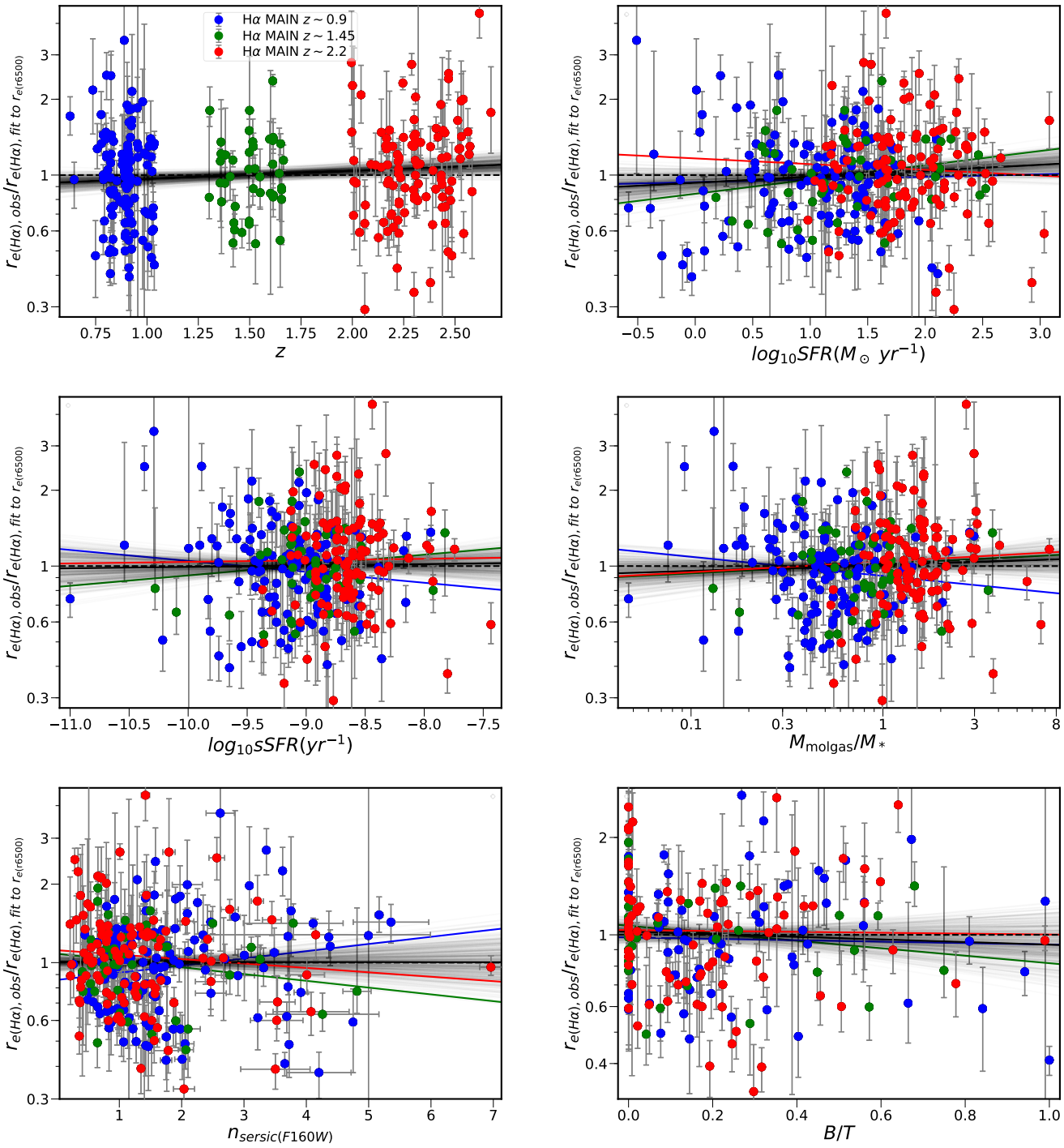

Figure 8. Residual Hα size with respect to the best fit versus continuum size (see Figure 7 top-left panel) versus redshift (top left), star-formation rate (top right), specific star-formation rate (middle left), molecular gas to stellar mass ratio (as inferred from Tacconi et al. (2018), middle right), Sersic parameter measured in the F160W band (bottom left), and bulge to total ratio (as measured by Lang et al. (2014) for a subset of our Hα MAIN sample, bottom right). The best fit and sample fits from MCMC are shown with the black solid line and fainter grey lines (and coloured lines for the three independent redshift bins). The black dashed line shows the level at zero residuals.

fits to stacked and circularised Hα profiles from the 3D-HST survey in stellar mass bins (outlined cyan circles, scaled to major axis sizes assuming an average ellipticity $\epsilon = 0.4$).

We now examine the importance of the second parameter in the lower panels. In each case we plot the residual of Hα size with respect to the best fit relation from the upper panel against the second parameter (i.e. left, versus stellar mass; right, versus continuum size) and then fit relations for these residuals. Here it is clear to see that the stellar mass adds nothing to the prediction of Hα size once the continuum size has been taken into account: the residual relation fits a slope consistent with zero and the intrinsic scatter drops only by 1% to 42±3%. On the other hand, the continuum size correlates well to the residual of Hα size at fixed stellar mass, with a slope of 0.71 ± 0.05 and an intrinsic scatter of 46 ± 3%, down from 68 ± 4% when fitting versus stellar mass only.

The stellar mass only has any relevance because it is correlated with the continuum size: once the correlation with continuum size is removed then there is no residual relation of Hα size with stellar mass. In other words, star-formation, on average, spatially tracks existing stars, but at fixed continuum size the global amount of stars has no relevance. The scatter of Hα size with stellar mass has a larger contribution from the 55% scatter between continuum size and stellar mass[25] than from the 43% scatter between Hα size and continuum size.

We divide the Hα MAIN galaxies into three subsamples of redshift, according to the KMOS band in which we observe the Hα emission line. These are $0.58 \leq z < 1.04$ (blue points, YJ band), $1.27 \leq z < 1.62$ (green points, H band) and $1.98 \leq z < 2.68$ (red points, K band). We also derive best fit relations for each of these sub-samples (coloured lines). Best fit slopes to the continuum size - Hα size relation of 0.93 ± 0.08 (YJ), 1.00 ± 0.11 (H) and 0.75 ± 0.09 (K) are consistent with our combined best fit relation within 2σ, and with close to a linear relation (with the possible exception of the highest redshift bin which is 2.8σ away).

The fit intercept corresponds to the typical Hα size of a galaxy at a particular continuum size: for a near linear relation this is a near constant ratio. We derive this ratio at the median continuum size of 3.23 kpc to be 1.18 ± 0.03, i.e. a median Hα size which is 18% larger than the continuum size. Folding in the measured intrinsic scatter, this corresponds to a mean Hα size which is 26% larger than the continuum size[26]. This compares to the typical size ratio of ~ 1.3 found by Nelson et al. (2012) in highly star forming 3D-HST galaxies at $z \sim 1$, and the median ratio from stacked profiles of normal star-forming 3D-HST galaxies (~ 1.1 Nelson et al. 2016a). Within our wide redshift range, there is no evidence for evolution in this value, with consistent best fit values of 1.13 ± 0.05, 1.17 ± 0.06 and 1.20 ± 0.05 in the three redshift bins defined above. So while Hα sizes do track existing stellar sizes they are, in a median (mean) sense, larger by ~ 18% (~ 26%) over our full redshift range. That star-formation sizes are larger than stellar sizes is a pre-condition for in-situ size-growth, and we shall return to this topic in Section 7.2.

[25] This value derived from our sample is fully consistent with the 56% found by vdW14.

[26] The mean of a log-normal distribution = median+$0.5\sigma^2$.

6.2. *Which other parameters influence* Hα *size?*

Figure 7 demonstrates that, at fixed galaxy continuum size, there is no significant residual dependence on redshift (when split into three bins). This is confirmed by directly fitting the residual to the Hα size – continuum size best fit against redshift (Figure 8, top left panel). We find only a marginal dependence on redshift at $< 2\sigma$ level, and the intrinsic scatter of the size-size relation does not drop when redshift is included as a third parameter.

In Table 1 we show the best fit slope β[27], the fraction of Monte-Carlo realizations with β greater than zero ($P(\beta > 0)$), the Spearman rank correlation coefficient (ρ) and the probability that it is consistent with the null (no-correlation) hypothesis ($P(\rho|null)$) for the residuals of the size-size relation versus several other parameters.

Having explored the role of continuum size, stellar mass and redshift, we now turn at examining the dependence on star-formation rate, and other quantities which are known to correlate with it. This is done in Figure 8, where we plot the size-size relation residuals vs the star-formation rate in the top right panel and specific star-formation rate in the middle left panel. In the middle right panel, we look at the residuals vs the ratio of inferred molecular gas mass to stellar mass, $M_{\rm molgas}/M_*$, estimated using the relation of Tacconi et al. (2018, their BEST sample as in their Table 3b) which depends on z, δ(MS) (logarithmic offset from the Whitaker et al. (2014) MS relation) and M_*. There is no significant trend in residual size with SFR, sSFR, $\delta(MS)$ or inferred $M_{\rm molgas}/M_*$, nor any notable decrease in scatter, suggesting that – at least for normally star-forming main sequence galaxies – the star-forming gas traces the stars in exactly the same way independent of the relative amount of star-forming gas or of star formation efficiency within the limits to which we can measure it.

In the bottom panels of Figure 8 we examine the dependence on galaxy morphology parametrized by the Sersic index of our fit in the F160W band, and the bulge to total ratio B/T from the fits of Lang et al. (2014)). The sample of Lang et al. (2014) partially overlaps with the Hα MAIN sample, with only 60% of the galaxies having a valid value of B/T. Nonetheless this subsample is large enough to derive statistically robust conclusions. As demonstrated in the figure and in the table, there is no significant dependence. his contrasts with the situation in the local Universe, where normally star-forming (gas rich) galaxies with little or no bulge tend to have very similar Hα and continuum sizes, whereas those with more significant bulges have relatively larger Hα sizes (Fossati et al. 2013). In galaxies with more bulge, the half-light size of the combined bulge+disk is less than that of the disk, and the Hα emitting gas usually shows little sign of a bulge component. Therefore it is perhaps surprising that our KMOS^{3D} galaxies with higher Sersic index or higher B/T measurements show no indication of relatively larger Hα sizes. Morphology does not seem to play a role in driving the relative size of the Hα disk in the high redshift Universe, at least not measurably

[27] With the symbol β we simply refer to the slope of the power-law fit and this parameter has no relation with the UV β slope.

Table 1
Correlation of offset from $r_e(H\alpha) - r_e(r6500)$ relation (Figure 7 top-left panel) with other parameters.

PARAMETER, X	β	$P(\beta > 0)$	ρ	$P(\rho \mid null)$
z	0.03 ± 0.02	0.978	0.115	0.05
$\log_{10}(M_*/M_\odot)$	0.04 ± 0.02	0.974	0.114	0.05
$\log_{10}(SFR(M_\odot\ yr^{-1}))$	0.02 ± 0.02	0.921	0.088	0.14
$\log_{10}(sSFR(yr^{-1}))$	0.01 ± 0.02	0.591	0.037	0.53
$\log_{10}(\delta(\mathrm{MS}))$[a]	-0.01 ± 0.03	0.424	−0.015	0.80
$\log_{10}(M_{\mathrm{molgas}}/M_*)$[b]	0.02 ± 0.03	0.767	0.075	0.21
$n_{Sersic,F160W}$	0.00 ± 0.01	0.496	−0.005	0.93
$B/T, F160W$[c]	-0.04 ± 0.06	0.249	−0.020	0.79
A_V	-0.03 ± 0.02	0.059	−0.08	0.18
$\log_{10}(L_{H\alpha,erg.s^{-1}})$ from fit[d]	0.11 ± 0.02	1.0	0.31	$< 10^{-5}$
$\log_{10}(\frac{SFR(M_\odot.yr^{-1})}{L_{H\alpha,erg.s^{-1}}})$ from fit[d]	-0.10 ± 0.02	0.0	−0.22	0.0001
$\log_{10}(\frac{SFR(M_\odot.yr^{-1})}{L_{H\alpha,erg.s^{-1}}})$ from fit[d] and dust-corrected[e]	-0.11 ± 0.03	0.0	−0.23	0.0001
$(U-V)_{\mathrm{rest}}$	-0.09 ± 0.06	0.080	−0.072	0.25
$(V-J)_{\mathrm{rest}}$	-0.09 ± 0.05	0.031	−0.091	0.13
ϵ[f]	-0.13 ± 0.14	0.171	−0.122	0.04
$\log_{10}([\mathrm{NII}]/H\alpha)$[g]	0.02 ± 0.07	0.594	0.074	0.34
$\log_{10}(\delta_{0.75})$[h]	-0.01 ± 0.03	0.36	−0.07	0.37
$\log_{10}(M_{h\mid cen,50\%}/M_\odot)$[i]	0.05 ± 0.03	0.96	0.09	0.12
P_{sat}[j]	-0.08 ± 0.05	0.07	−0.07	0.23

NOTES. Best fit between the parameter given in the first column (X) and the residual Hα size relative to the best fit versus continuum size for the full Hα MAIN sample ($Y = \frac{r_{e(H\alpha),\mathrm{obs}}}{r_{e(H\alpha),\mathrm{fit}}}$). Fits are of the form $Y = 10^{\alpha+\beta.X}$, with the slope β and $1-\sigma$ errors given in column 2. In column 3, $P(\beta > 0)$ is estimated from the fraction of MCMC realizations with a positive slope, so values around 0.5 are random, while values of 0 or 1 indicate a significant negative or positive slope respectively. Column 4 contains the Spearmann rank correlation coefficient, and column 5 indicates the probability (p-value) of such a value assuming no correlation between the two parameters.

[a] $\delta(\mathrm{MS}) = \mathrm{SFR}(M_\odot.\mathrm{yr}^{-1})/\mathrm{SFR}_{\mathrm{MS,z,M_*}}(M_\odot.\mathrm{yr}^{-1})$ with the parametrizations of the MS from Whitaker et al. (2014).

[b] Inferred via $\log_{10}(M_{\mathrm{molgas}}/M_*) = -1.25 + 2.6log_{10}(1+z) + 0.53log_{10}(\delta(\mathrm{MS})) - 0.36\log_{10}(M_*)$ (Tacconi et al. 2018, best fit relation).

[c] Restricted to galaxies with valid B/T measurements in the F160W band from Lang et al. (2014).

[d] $L_{H\alpha,erg.s^{-1}} = 2\pi.h^2.I0.(1.-\epsilon)$

[e] Using the differential dust recipe of Wuyts et al. (2013): $\log_{10}(L_{H\alpha,erg.s^{-1},\mathrm{dust.cor}}) = \log_{10}(L_{H\alpha,erg.s^{-1}}) + 0.4(1.9A_{\mathrm{cont}} - 0.15A^2_{\mathrm{cont}})$

[f] Galaxy ellipticity, ϵ from fit to F160W band.

[g] Restricted to galaxies in the Hα MAIN sample for which the skyline residual contamination at the wavelength of the red [NII] emission line is not strong.

[h] Environmental overdensity in 0.75 Mpc apertures from Fossati et al. (2017).

[i] 50%ile of probability distribution function for halo mass assuming the galaxy is the central of its halo from Fossati et al. (2017).

[j] Probability galaxy is a satellite, as calibrated by Fossati et al. (2017).

within our star-forming sample.

In Table 1 we test even more parameters, including those related to the dust extinction, the galaxy color, the ratio of SFR to Hα luminosity, the ratio [NII]/Hα, and the galaxy environment (parametrized by the local galaxy overdensity, halo mass, and probability of being a satellite galaxy from Fossati et al. (2017)).

Our analysis shows that most parameters show little or no correlation with the residual Hα size, and the only significant trends are those related to dust extinction which we discuss further in Section 6.4. None of these results are significantly changed if we restrict ourselves to the Hα BEST sample, eliminate galaxies hosting AGN or broad line emission, or limit to the stellar mass range of our highest redshift bin ($\log_{10}(M_*/M_\odot) \gtrsim 10$).

6.3. *Caveats*

In detail, the picture is more complicated. While much of the Hα emission locally traces the ionizing star-formation, there can be a more diffuse component, additional sources of ionization, and much of the emission can be obscured by dust, especially in dense and infrared-bright starbursting regions. For example, two very high mass star-forming galaxies in our sample (U4_20704 and U4_36247 at $M_* > 10^{11}\,M_\odot$) which have been observed by ALMA at 870μm (Tadaki et al. 2017) to have significantly smaller submillimeter sizes than their Hα or F160W sizes.

Also the continuum emission, which we have corrected to rest frame 6500Å to remove the effects of a variable rest frame wavelength for galaxies at different redshifts, does not perfectly trace the stellar mass in the galaxy. We examine the Sersic profile fits to stellar mass maps produced by Lang et al. (2014) for $0.5 < z < 2.5$ and $M_* > 10^{10}\,M_\odot$ galaxies in our sample. We find for $n_{\mathrm{Sersic}} < 2$ galaxies that half-mass sizes are on average $\sim 75-80\%$ of the rest frame 6500Å half-light sizes with a $< 5\%$ dependence on redshift, consistent with Wuyts et al. (2012, their Figure 11). The ratio $r_{e(M_*)}/r_{e(r6500)}$ decreases for high n_{Sersic} sources in our lower redshift bin, possibly demonstrating the influence of a higher mass-to-light ratio bulge in such galaxies. However, as shown in Figure 9, we find no correlation between $r_{e(M_*)}/r_{e(r6500)}$ and $r_{e(H\alpha)}/r_{e(r6500)}$, demonstrating that the driver of

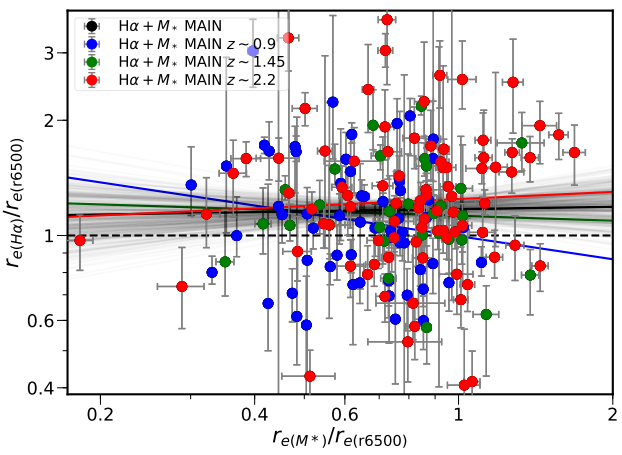

Figure 9. Ratio of the half-mass (from Lang et al. 2014) to the half-light size versus the ratio of the Hα size to the half-light size. Points and lines are color coded as in Figure 8. The lack of a significant correlation demonstrates that whatever drives variations in $r_{e(M_*)}/r_{e(r6500)}$ is not driving variations in $r_{e(H\alpha)}/r_{e(r6500)}$.

variations in $r_{e(M_*)}/r_{e(r6500)}$, such as large bulges in some galaxies at lower z, is not driving variations in $r_{e(H\alpha)}/r_{e(r6500)}$. This suggests that, in our observed continuum band and for the normally star-forming galaxies in our sample, we are predominantly tracing the disk and we are measuring disk sizes, even in galaxies with significant bulges.

The colour gradients in late-type galaxies appear likely to result predominantly from gradients in dust extinction (Pastrav et al. 2013). In this case, any dust gradient will effect the extinction gradient for Hα emission as well as the continuum. Under the foreground screen approximation, these are equally affected, and the ratio of half-light sizes should be unaffected. However, as we shall see in Section 6.4, there is excess extinction of Hα emission associated to dust embedded in the star-forming HII regions, well described on average by differential extinction laws such as Wuyts et al. (2013). The dustier part of the galaxy (typically the centre, Wuyts et al. 2012; Nelson et al. 2016b) will have extra extinction in Hα compared to continuum implying that, while both observed sizes will be larger than the true size, the Hα size should be increased by a larger amount. In other words, the ratio of Hα to continuum size should be an upper limit for the ratio of the size of the star-forming disk to that of the stellar mass disk.

6.4. *Dependence on dust*

The left hand panel of Figure 10 examines the dust correction. On the x-axis we plot the best fit A_V extinction estimated as part of the SED fits to multiwavelength photometry (Wuyts et al. 2011). On the y-axis we plot the ratio of the total SFR to the total Hα luminosity from KMOS. The SFR is estimated by Wuyts et al. (2011) and includes obscured star-formation as seen via infrared emission from *Herschel*/PACS or *Spitzer*/MIPS where detected, and is based on SED fits where there is no infrared detection. The total Hα luminosity is estimated by integrating the IMFIT exponential disk fit out to infinity. Similar results are obtained by integrating the Hα image (these are merely noisier and truncated at the edge of the KMOS field of view).[28] The y-axis value can therefore be interpreted as a conversion factor from Hα luminosity to total SFR including the dust correction. A standard conversion *not including dust* from Kennicutt (1998), shifted to a Chabrier initial mass function (IMF), describes the lower envelope of the data well (horizontal dashed red line). As A_V increases, so does the dust correction to this conversion factor (effectively the mass of stars formed per number of detected Hα photons). If the Hα extinction was equivalent to the continuum extinction at the wavelength of Hα, $A_{cont} = 0.82A_V$ from Calzetti et al. (2000) as in Wuyts et al. (2013), (as appropriate in the case of a foreground dust screen) we would get the dashed green line. Our best fit to the data (black dashed line) implies a steeper dependence on A_V, and is in good agreement with the best fit polynomial from Wuyts et al. (2013) (blue dashed line), implying an excess extinction A_{extra} for the Hα emission in HII regions such that $A_{H\alpha} = A_{cont} + A_{extra}$ with $A_{extra} = 0.9A_{cont} - 0.15A^2_{cont}$.

In the right hand panel of Figure 10 we show that there is only a weak, barely significant negative correlation between the residual Hα size at fixed continuum size and A_V, implying little or no correlation between the integrated continuum obscuration and the extent of Hα emission at fixed continuum size in the galaxy, as confirmed in Table 1. Similarly weak correlations are found with rest frame galaxy colours. The lack of a stronger correlation contrasts with simple expectations. Galaxies exhibit a centrally peaked dust extinction profile (e.g. Wuyts et al. 2012; Nelson et al. 2016b) and an excess integrated extinction at Hα increasing with increasing A_V as observed in the left panel of Figure 10. This implies that we expect extinction effects to drive a flattening of the light profiles (larger half-light radius observed than the true one, see e.g. Pastrav et al. 2013), and that this applies more in galaxies with higher extinction (A_V) and more in Hα than in continuum ($A_{H\alpha} > A_V$). As a result, the ratio of observed Hα to continuum size should be larger than the true one and, naively, one might expect that this effect should increase with increasing A_V. Instead we see only a very weak – and negative – correlation of observed Hα to continuum size ratio (at fixed continuum size) with A_V.

In contrast, Figure 11 shows how the residual Hα size at fixed continuum size does depend upon the parameters specifically related to the dust obscuration of the Hα emission. The upper panel shows the variation as a function of the total obscuration of Hα emission, as parameterized via the ratio of the total SFR to Hα luminosity (the y-axis parameter from Figure 10). In the lower panel we correct the Hα luminosity for the average Hα dust extinction using the well-fit prescription from Wuyts et al. (2013). Now the x-axis values describe the *residual dust-correction* to Hα emission after applying this average correction. In both panels of Figure 11, the vertical dashed green line refers to the Kennicutt (1998) conversion between SFR and (extinction-corrected) Hα luminosity.

[28] Note: these estimates are both in excellent agreement with the aperture values presented by W19, for which the clearest difference is the expected dependence on the ratio of effective radius to aperture size.

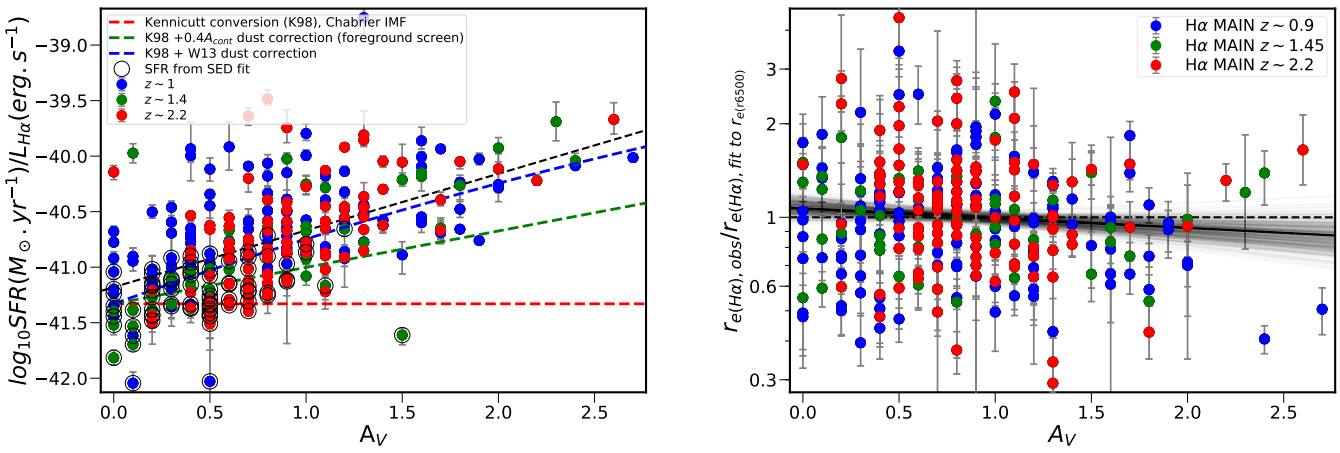

Figure 10. Left: Compares the integrated dust obscuration of the stars with that of Hα emission tracing SFR. The x-axis value A_V is estimated assuming a foreground dust screen from SED fitting (Wuyts et al. 2011), while the y-axis is the ratio of the total estimated SFR (from IR+UV where available or SED otherwise) to the total Hα luminosity from the exponential fits. The horizontal dashed red line denotes the canonical calibration of SFR to $L_{\rm H\alpha}$ from Kennicutt (1998), assuming a Chabrier initial mass function (IMF) of stars. Assuming star-formation is obscured to the same degree as older stars, we get the dashed green line. An additional component of extinction as empitically calibrated by Wuyts et al. (2013) is shown as the blue dashed line. This comes very close to our best fit relation (black dashed line). Galaxies with no IR detection and therefore with SFR from SED fits are outlined with black circles: clearly these are the less dusty objects. Right: The dependence of the residual Hα size at fixed continuum size on A_V is weak and not highly significant.

The typical residual Hα size (at fixed continuum size) increases significantly for less total extinction of Hα, even after correction for the average global obscuration, $A_{\rm H\alpha}(A_V)$ based on the Wuyts et al. (2013) recipe. The lack of dependence of residual Hα size on continuum obscuration (Figure 10 right panel) implies that, moving from the top to the bottom panel of Figure 11, the trend is barely reduced by a global A_V-based correction. In other words, the relative Hα size at fixed continuum size must be largely independent of the total amount of foreground dust obscuration $\propto A_V$. Instead our results must be interpreted to mean that the ratio of Hα to continuum obscuration $A_{\rm H\alpha}/A_V$ decreases for galaxies which are relatively more extended in Hα relative to stars.

We have seen no notable dependence of residual Hα size at fixed continuum size on global parameters A_V, SFR or inferred gas fraction. That the residual Hα size *decreases* with increasing $A_{\rm H\alpha}/A_V$, must originate in the internal geometries of dust differently affecting young and old stars in galaxies. Fitting a dust model to explain correlations with the resolved extinction maps of low redshift MaNGA galaxies, Li et al. (2019) derive a best fitting model in which the fraction of dust in a foreground screen increases with galactic-centric radius, with the rest of dust assumed to live in Hα-emitting HII regions. Such a model implies that Hα photons escape relatively more easily at large galactic-centric distances than in the centre of galaxies, and that galaxies with intrinsically large Hα disk sizes or steep dust obscuration profiles are less subject to extra obscuration of Hα emission.

This would put such galaxies below the average relation in the left panel of Figure 10 (blue dashed line), closer to a the pure foreground screen model, and also to the left of both panels in Figure 11. These results are also tabulated in Table 1 and we find equivalent trends at similar significance if we use the total Hα luminosity from integrated Hα maps instead of the integrated exponential fit. This demonstrates that the trends are not driven by covariance in the fitting parameters.

Finally we note that despite the details of these trends, the overall effect of dust obscuration is still to increase the observed Hα sizes more than that of the stars, with no difference only in the limiting case of no embedded dust (pure foreground screen). In other words, the measured mean (median) size ratio of 1.26 (1.18) is likely to be an upper limit on the true average ratio of the star-forming disk size to the stellar disk size. Indeed, in extreme cases from within our sample we know that there are highly star-forming massive galaxies hosting strong central star-formation (Tadaki et al. 2017) which is almost completely obscured in Hα. However, it appears that the Hα sizes of such galaxies are nonetheless similar to that of their stars. Indeed, we see a relatively unobscured and sub-dominant component of star formation which is associated to the stellar disk while the majority of star-formation occurs in highly optically thick central region of the galaxy, with little or no escape of ionizing photons and subsequent Hα emission.

7. INTERPRETATION

In the previous Section we have found that over the large redshift and stellar mass range probed by our observations, the ionized gas size is on average 1.26 times larger than the continuum size (tracing older stellar populations), with negligible dependence on other fundamental parameters. We now interpret these results in terms of gas accretion and its angular momentum.

7.1. *Analytic considerations*

A simplified prediction for disk sizes can be derived by combining equations 2 and 12 of Mo, Mao & White (1998):

$$R_d \propto H(z)^{-2/3} \cdot \lambda' \cdot M_{halo}^{1/3} \qquad (6)$$

for disk size R_d, galaxy spin parameter $\lambda' = \lambda \cdot \frac{j_d}{m_d}$, halo spin parameter λ, a fraction of halo angular momentum

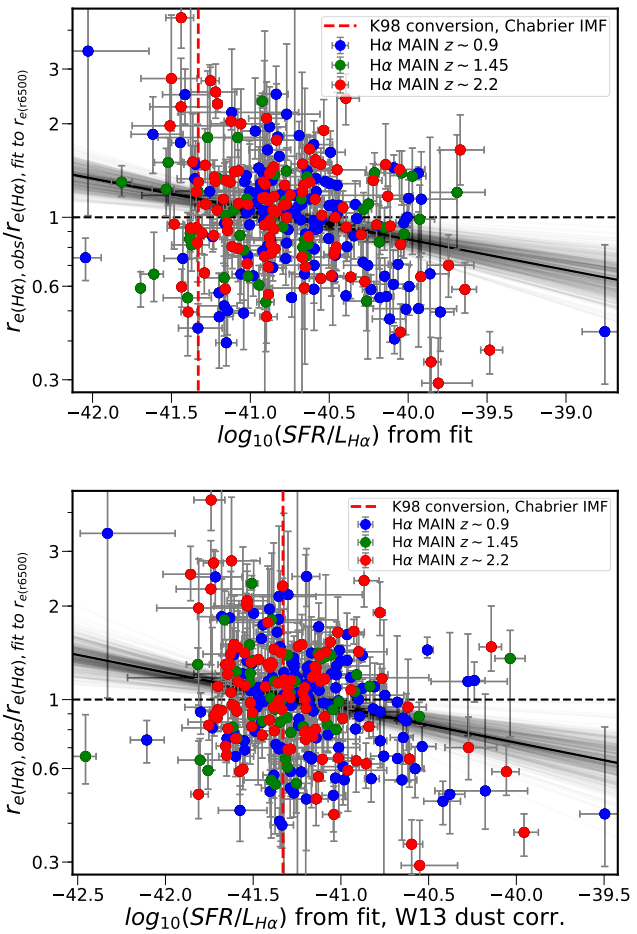

Figure 11. Residual Hα size at fixed continuum size versus the amount of Hα dust obscuration. The upper panel shows the relation to the total SFR normalized by total Hα luminosity (y-axis value in Figure 10, left panel). The bottom panel corrects this Hα luminosity for extinction as a function of A_V using the differential extinction law of Wuyts et al. (2013) (the blue line from Figure 10) and examines the correlation of residual Hα size at fixed continuum size with the residual Hα extinction. Even this residual dust extinction correlates significantly with the residual Hα size, indicating that galaxies with less Hα extinction at fixed A_V can be visibly more extended in Hα relative to their stars. Our best fit relations between parameters are shown (black solid line), as well as individual Monte-Carlo realizations (fainter grey lines).

in the disk j_d and of halo mass in the disk m_d (such that $j_d/m_d = 1$ where there is no difference in the specific angular momentum of disk and halo). R_d can then be related to the disk mass M_d via $\mathrm{M_{halo}} = (\mathrm{M_d}/\mathrm{m_d})$.

The predicted dependence on $\mathrm{M_{halo}^{1/3}}$ originates with the predicted proportionality to the circular velocity of the halo, $\mathrm{V_c}$, and thus $\mathrm{M_{halo}^{1/3}}$ from the Virial theorem. This is steeper than the observed dependence on stellar mass in the Tully-Fisher relation ($\sim 1/3.75 \sim 0.27$ Lelli, McGaugh & Schombert 2016), which is more in line with the slope of the stellar mass - size relation (~ 0.22, vdW14). A slope of less than 1/3 may be accounted for by variations in m_d with mass. The predicted dependence on $H(z)$, on the other hand, suggests a strong evolution in galaxy sizes at fixed mass. Observations are at potential odds with one another about the rate of evolution. vdW14 find that observed median sizes of star forming disk galaxies at fixed stellar mass evolve as $H(z)^{-2/3}$ but Suess et al. (2019) claim to see little evolution at fixed stellar mass of half-mass sizes, once they account for radial gradients in the mass to light ratio. Both cases appear surprising, as disk sizes are likely to be set at the epoch of formation (not observation) but still evolving as they grow through star formation. That Suess et al. (2019) find a much flatter dependence on stellar mass also begs questions about the expected dependence of size on mass or circular velocity.

More straightforwardly, the measured intrinsic scatter in galaxy sizes of $1\sigma \sim 0.16 - 0.19$ dex is very consistent with the scatter in continuum galaxy size at fixed specific angular momentum Burkert et al. (2016), and with the scatter in halo spin parameter from simulations. The latter similarity suggests that most of the scatter in galaxy sizes originates as scatter in the halo spin.

Equation 6 can also be applied to examine the star-forming disk size, noting that the parameters j_d and m_d effectively describe the efficiency of angular momentum and mass transfer from halo to disk. The term $\mathrm{M_{halo}^{1/3}}$ in equation 6 describes the gravitational potential at the time of formation of the relevant component. Therefore we can predict the ratio of star-forming disk size to stellar disk size:

$$\frac{R_{d,SF}}{R_{d,*}} \propto \left(\frac{H(z_{SF})}{H(z_*)}\right)^{-2/3} \cdot \frac{\lambda'(z_{SF})}{\lambda'(z_*)} \cdot \left(\frac{M_{halo,z_{SF}}}{M_{halo,z_*}}\right)^{1/3} \quad (7)$$

where the Hubble parameter, specific angular momentum, and halo mass should be evaluated at times appropriate to the star-forming and stellar components. Naively, equation 7 suggests that the star-forming disk should be larger than the stellar disk by an amount depending upon the Hubble parameter at their relative times of formation with $z_{SF} << z_*$, with modifications that can relate to the growth in halo mass, and to changes in the halo spin parameter over time.

We found that the size in Hα emission correlates strongly with the continuum size, with an intrinsic scatter smaller than that of continuum size – and of inferred halo spin parameters – at fixed mass. This demonstrates the stability over time of the spin parameter, with less variation in time than variation between halos. The intrinsic scatter of $43 \pm 3\%$ combines any short term temporal variation in λ with the changes in the efficiency of the angular momentum transfer from halo to disk scales including the process of star-formation, as well as the effects of dust on both size measurements. We evaluate the ratio $R = [H(z_*)/H(z_{SF})]^{2/3}$ appearing in equation 7 at redshifts $z_{SF} = z_{obs} = 1$ and 2, upon which our observations are concentrated. Then with the assumed cosmology we obtain $R = 1.33$ for $z_* = 1.5$ and $z_{obs} = 1$, and $R = 1.59$ for $z_* = 3$ and $z_{obs} = 2$, where the z_* values are selected to have a roughly constant lookback time of 1 Gyr from the observation redshifts. On this timescale a galaxy would double its stellar mass, since $M_*/SFR \lesssim 1$ Gyr for $z > 1$. We then evaluate the last term of equation 7, $P = [M_{halo,z_{SF}}/M_{halo,z_*}]^{1/3}$ using the halo growth factor $(1 + 1.11z) \cdot \sqrt{\Omega_M.(1+z)^3 + \Omega_\Lambda}$ given by Fakhouri, Ma & Boylan-Kolchin (2010). We get $P = 0.8(0.7)$ with the same choice of z_* and z_{obs} made above, respectively. In summary, equation 7 gives

Table 2

$log_{10}\frac{M_*}{M_\odot}$ AT $z=1$	$log_{10}\frac{M_*}{M_\odot}$ AT $z=2$	
	SF	SF + mass loss
10	8.02	8.63
10.5	8.76	9.38
11	9.95	10.47
11.5	10.96	11.20

NOTES. $z=2$ progenitor galaxy mass of a given $z=1$ galaxy in our toy model. Stellar mass growth via star-formation occurs along the main sequence (Whitaker et al. 2014). In the third column we include stellar mass loss in the calculation, which offsets star-formation such that the mass growth is reduced. Galaxies below $M_* \sim 10^{10.8}\,M_\odot$ at $z=1$ had stellar masses below $10^{10}\,M_\odot$ at $z=2$, and below our approximate KMOS^{3D} limit.

$R_{d,SF}/R_{d,*} \sim 1.11(1.06)\cdot\lambda'(z_{SF})/\lambda'(z_*)$, respectively. The simplest interpretation of the observed lack of evolution in the ratio of star-forming size (as traced by Hα) to that in stars (as traced in the rest frame 6500 Å), as seen in our data, is therefore that the specific angular momentum of star-forming material is stable across many Gigayears of cosmic time, resulting in an almost constant $\lambda'(z_{SF})/\lambda'(z_*)$ ratio. This evidence can be physically related to the complex interplay of cooling, accretion, star-formation and feedback which might regulate the angular momentum of star-forming material and its evolution.

7.2. *A toy model for evolution in size and mass*

Observed star-forming galaxies have star-formation rates and stellar sizes which depend upon their stellar mass and redshift, with log-normal scatter around the observed relations. In this section we construct a simple toy model to predict how star-formation in galaxies should lead them to evolve in the size-mass plane.

Our model predicts the evolution in a galaxy's stellar mass by assuming it to grow purely via star-formation according to the main sequence relation between SFR and stellar mass from Whitaker et al. (2014). We include the log-normal scatter ~ 0.3 dex (Noeske et al. 2007) to get estimates of mean SFR rather than median SFR, which should be appropriate assuming individual galaxies scatter above and below the main sequence. This is offset by mass loss from stars computed according to the Flexible Stellar Population Synthesis (FSPS) code (Conroy, Gunn & White 2009). Table 2 provides the stellar mass at $z=2$ for galaxies evolved in this way and ending with fixed masses of $\log_{10}(M_*/M_\odot) = 10, 10.5, 11, 11.5$ at $z=1$. We also compute the much lower $z=2$ stellar mass for a star-formation only recipe (no mass loss, and thus much more rapid mass evolution). Galaxies below $M_* \sim 10^{10.8}\,M_\odot$ at $z=1$ had stellar masses below our approximate KMOS^{3D} limit of $10^{10}\,M_\odot$ at $z=2$.

Motivated by the consistent ratio of Hα to continuum sizes $r_{e(H\alpha)}/r_{e(r6500)}$ in our data, and in particular the lack of significant mass or redshift dependence, we assume a constant value in the ratio of star forming to stellar size $r_{e(SF)}/r_{e(M_*)}$ which we call the size growth factor. A galaxy starts with an exponential profile at high redshift. This profile is evolved self-consistently over many small steps in time. At each step, the newly formed stars are generated with an a radial distribution described by an exponential profile and a half-mass size equal to the current stellar half-mass size multiplied by the size growth factor. Stellar mass loss is self-consistently tracked as a function of the stellar age, such that mass is removed from the radii at which it was added when those stars formed i.e. stars are assumed to remain on their initial, circular orbits. The profile evolves in this way, driving growth in the stellar disk with time. The evolving profile retains a roughly exponential form but with slowly changing scale-length with radius ($n_{\rm Sersic} - 1 > 0$ but is small) such that the inner ($r << r_e$) profile, dominated by old stars, is consistent with an exponential with half-light radius $= r_{e(M_*)}$, and the outer ($r >> r_e$) profile, dominated by young stars, is consistent with an exponential with half light radius equal to $r_{e(M_*)} \times (r_{e(SF)}/r_{e(M_*)})$.

Figure 12 shows the toy model evolution of a galaxy with size growth factor $\frac{r_{e(SF)}}{r_{e(M_*)}} = 1.26$ and final stellar mass $\log_{10}(M_*/M_\odot) = 11$ at $z=1$. Recall that dust considerations in Section 6.4 indicate that $\frac{r_{e(SF)}}{r_{e(M_*)}} = 1.26$ should be an upper limit. We examine the evolution in stellar mass and size (focused on redshifts $1 < z < 2$) and in the stellar mass vs size plane[29]. A simple empirical estimate suggests the fractional mass evolution goes as the specific star-formation rate, while the fractional radial evolution goes as the specific star-formation rate times the size growth factor (ignoring mass-loss and the mildly non-exponential nature of evolving profiles) . With this recipe, the rate of change of log size with respect to the change in log mass is the natural logarithm of the size growth factor: i.e. $\Delta(\log r_e) \sim \ln(\frac{r_{e(SF)}}{r_{e(M_*)}}) \times \Delta(\log M_*)$ (blue line in Figure 12). This approximation is close to our numerically derived slope, especially in the no mass loss case (age-dependent mass loss leads to mildly non-linear effects).

In the bottom-right panel of Figure 12 we examine how the toy model evolution with different size growth factors compares to the measured evolution of the size-mass relation for late type (star-forming) galaxies, from vdW14, interpolated between the tabulated midpoints of redshift bins at $z=1$ and $z=2$, and corrected to rest-frame 6500Å for consistency with our observed sample. This choice of observed relation is discussed further in Section 7.3.

Our evolutionary tracks are fixed such that they result in a galaxy of $\log_{10}(M_*/M_\odot) = 11$ at $z=1$ and with a size defined by the $z=1$ size-mass relation of vdW14. Evolving up to this fixed point, we find that a size growth factor close to our upper limit value of 1.26 is required merely to evolve galaxies *along* the size-mass relation. With smaller values, the sizes of star-forming galaxies at fixed stellar mass would actually *decrease* with increasing cosmic time. These results suggest that growth via star-formation is unlikely to grow galaxies enough in size to do more than retain a non-evolving size-mass relation and almost certainly not explain such a strong evolution as observed by VdW14.

In Figure 13 we study the ratio of $z=1$ to $z=2$ size as a function of the size growth factor for galaxies resulting in a galaxy of a particular mass at $z=1$ and with a size

[29] For simplicity in this section the simple notation r_e is frequently used to refer to the half mass size $r_{e(M_*)}$.

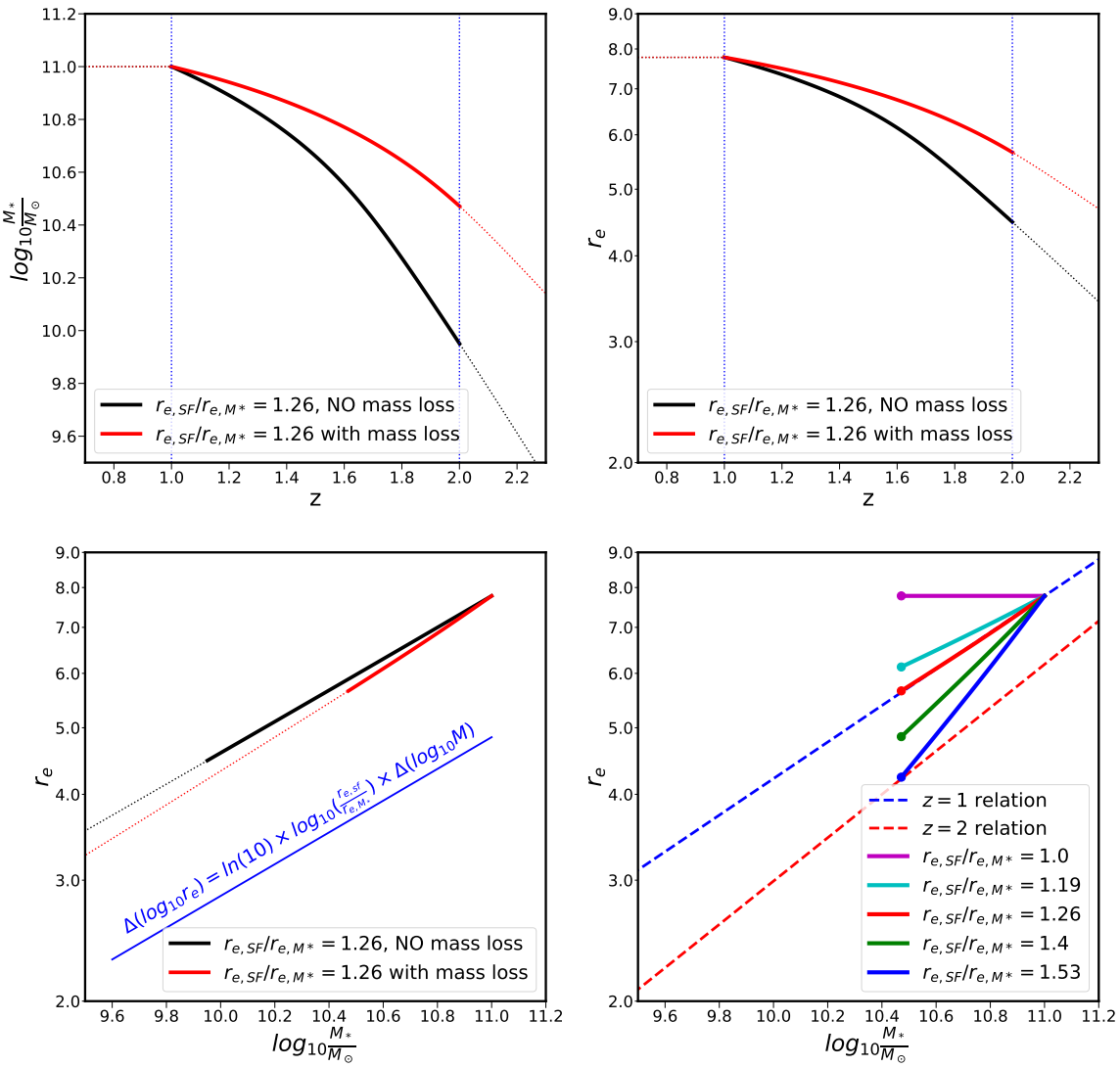

Figure 12. Toy model evolution of a galaxy with size growth factor $r_{e(SF)}/r_{e(M_*)}$ = 1.26 in stellar mass (top-left panel), stellar size (top-right panel) and the evolutionary track in stellar mass vs size (bottom-left panel). Tracks are shown for models with (red) and without (black) mass loss. Thicker, solid lines refer to the evolution between $z = 2$ and $z = 1$. Including mass loss significantly reduces the rates of growth in both mass and size, without much changing the evolutionary track in mass vs size. A good analytic approximation for the size evolution is shown in the bottom-left panel (blue line). Bottom-right panel: Toy model growth from $z = 2$ to $z = 1$ as in the previous panel, but for different values of the size growth factor $r_{e(SF)}/r_{e(M_*)}$. Galaxies are evolved using our toy model and end by design on the $z = 1$ size-mass relation of star-forming (LT) galaxies from vdW14 corrected from F160W to rest-frame 6500 Å using the Kelvin et al. (2012) recipe (blue dashed line). The evolution of galaxy size depends upon the size growth factor $r_{e(SF)}/r_{e(M_*)}$ as depicted by the solid evolutionary track lines. A very large size growth factor $r_{e(SF)}/r_{e(M_*)} \sim 1.53$ is required to reproduce the observed evolution, from the $z = 2$ LT size-mass relation of vdW14 (red dashed line), while if we assume size growth factors equivalent to our measured mean (median) observed values $r_{e(H\alpha)}/r_{e(F160W)} = 1.26$ (1.19), these are barely enough to evolve a galaxy *along* a non-evolving size-mass relation.

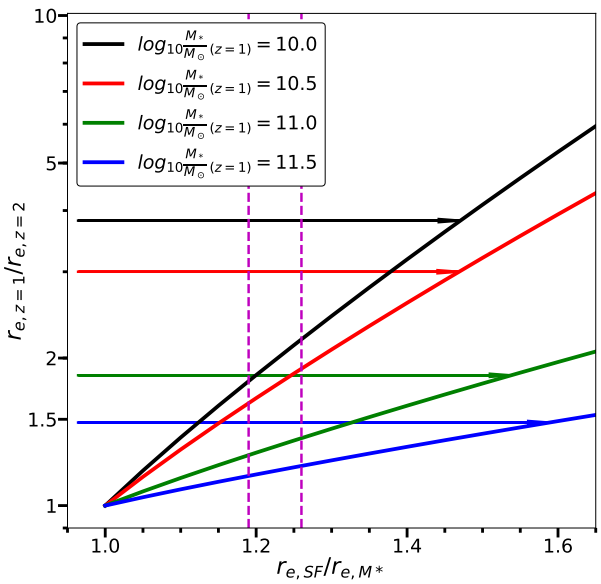

Figure 13. Total size growth in our toy model from $z = 2$ to $z = 1$ for galaxies with four values of final stellar mass at $z = 1$ (coloured lines, see legend). Sizes are assumed to grow exclusively via the formation of new stars with a constant size growth factor $\mathrm{r_{e(SF)}}/\mathrm{r_{e(M_*)}}$ (x-axis), and with a mass evolution following the star-formation main sequence. The arrows denote the equivalent size growth of the same galaxy over the same redshift interval from the size-mass relation of vdW14, and point to the place where this growth is reached by our size growth model. These values are much larger than those measured in our sample (vertical, dashed magenta lines show the median and mean values at 1.19 and 1.26). This suggests that star-formation driven size growth is not enough to explain the observed size evolution of star-forming galaxies.

defined by the $z = 1$ size-mass relation of vdW14. The arrows point to the location where the model size growth matches the observed growth for the average star-forming galaxy. We examine four final ($z = 1$) galaxy masses $10 \leq \log_{10}(M_*/\mathrm{M}_\odot) \leq 11.5$. Although the progenitor galaxies at $z = 2$ would not make our KMOS^{3D} sample for the lower two mass bins (Table 2), it is still useful to examine predictions from our model under the assumption that the mass and redshift independence of the size growth factor extends to lower mass. The two vertical lines correspond to the median (1.19) and mean (1.26) values of $\mathrm{r_{e(H\alpha)}}/\mathrm{r_{e(r6500)}}$ from our analysis, respectively.

In all mass bins considered a very large size growth factor is required for galaxies to grow sufficiently to evolve from the $z = 2$ size-mass relation onto the $z = 1$ size-mass relation, assuming the vdW14 late type relations. This also increases with mass, from $\mathrm{r_{e(SF)}}/\mathrm{r_{e(M_*)}} \sim 1.50$ at $\log_{10}(M_*/\mathrm{M}_\odot) = 10$ to ~ 1.60 at $\log_{10}(M_*/\mathrm{M}_\odot) = 11.5$.

7.3. *Considerations and constraints on evolution*

To understand our constraints, we should consider a couple of apparent contradictions, and how to resolve them.

1. vdW14 determine an evolution in late type galaxy sizes at 5000Å at fixed stellar mass of $\sim H(z)^{-2/3}$, and an (almost un-evolving) dependence on stellar mass of $M_*^{0.22}$. Suess et al. (2019) find little dependence on stellar mass or redshift in *half-mass* sizes, accounting for gradients in the stellar mass to light ratio. Little redshift or mass-dependent evolution in sizes indicates little or no growth in size.

2. Without star formation driven size growth, there would be no age-gradients in galaxies, contradicting the idea of larger sizes at shorter wavelengths due to the increasing importance of younger stellar populations. Instead, our results *do* support the idea that newly forming stars populate a slightly larger disk than older stars.

3. A constant size growth factor $\frac{\mathrm{r_{e(SF)}}}{\mathrm{r_{e(M_*)}}}$ as a function of size, mass and redshift would imply a scale-free growth such that, while younger stars can be found on average at larger galactic-centric distances than older stars, the ratio of the two is independent of redshift and galaxy mass: we do not detect significant deviations from this constant growth. If true, there should be no epoch at which age gradients should disappear without invoking complex age-dependent radial migration. This appears to contradict the lack of M/L gradients at $z = 2$ seen by Suess et al. (2019).

   We do also find a greater difference between mass and light sizes in galaxies with higher sersic index, but only at $z \sim 1$ (not $z \sim 2$). This suggests a role for bulges, more prevalent at lower redshift, and driving greater M/L gradients in some galaxies. We note that in general star-forming disks may grow while overall galaxy sizes stay the same due to an increasing bulge contribution: due to the differing contributions of bulge and disk to light and mass, the bulge is more likely to dominate in mass, while more size growth may be seen in light.

4. On the other hand in Figure 9 we found no correlation of $\mathrm{r_{e(H\alpha)}}/\mathrm{r_{e(r6500)}}$ with $\mathrm{r_{e(M_*)}}/\mathrm{r_{e(r6500)}}$. This strongly suggests that whatever drives the gradients in M/L (such as age and bulge contributions) is not the dominant factor driving variations in $\mathrm{r_{e(H\alpha)}}/\mathrm{r_{e(r6500)}}$. We argue that these are driven instead mainly by variations in the gradient of dust and in particular embedded dust in star forming disks. Continuum light and Hα are therefore more closely tied than mass and Hα, and the ratio should remove the effect of a foreground dust screen but not of embedded dust.

Taking account of these considerations, we selected to compare to the simpler, light-based vdW14 relations. Considering our results, we cannot match the observed evolution of size-mass relations from vdW14. This would suggest that other physical processes for growth of star forming galaxies might be at play, and we will discuss candidates in the next section. However the results of Suess et al. (2019) suggest that evolution might not be so steep if we assume there is also a role for evolution in the mass to light gradients (even if this is driven in part by bulge formation). Such milder evolution can be consistent with our upper limit of $\sim 26\%$ for the size growth factor.

7.4. *Physical origins of galaxy size growth*

Equation 6 conveniently separates the dependencies on redshift and mass in the derivation of disk size for star-forming galaxies. In this context the mass-dependence is simply an imprint of the dependence of galaxy size on $\left(\frac{M_d}{m_d}\right)^{1/3} = M_{halo}^{1/3} \propto V_c$ and thus an imprint of the Tully-Fisher relation between galaxy mass and circular velocity. As star-formation appears to drive evolution approximately along this relation, this implies that the integrated growth in size and mass can be described by Equation 6, with $R_d \propto (M_d/m_d)^{1/3}$ and thus with $M_{halo}^{1/3}$, but with galaxy sizes scaled to the Hubble parameter at the epoch of observation, $H(z_{obs})$ such that there is no redshift dependence of the size growth factor (Equation 7). The measured size evolution of the size-mass relation by vdW14 on the other hand, scales as $H(z_{obs})^{-2/3}$ (or alternatively as $(1+z)^{0.75}$. Although this evolution might be overestimated in light-weighted sizes (see Section 7.3), if real it would suggest another form of growth not associated to star-formation – i.e. that the stellar component of star-forming galaxies does not retain its initial size, but rather evolves in size as predicted by Equation 6 due to angular momentum transfer with the surrounding material (gas and dark matter, see e.g. Struck & Elmegreen 2017). In addition, as we discuss below, *any* measured evolution of the size - mass relation is likely to be an overestimate, given that many of the more compact massive galaxies have their star-formation quenched between epochs.

The constant size growth factor, with no obvious dependence on redshift, size, and stellar or gas mass, implies that the model star formation driven size growth as seen in Figures 12 and 13 applies under widely varying conditions. While this may simply reflect the halo mass growth, the small intrinsic scatter (43%) also implies that the halo spin parameter λ remains very stable over time, and that the specific angular momentum transfer ($\frac{\lambda'}{\lambda} = \frac{j_d}{m_d}$ in Equation 6) is also quite insensitive to a wide variety of halo growth rates and physical conditions. Such stability can be achieved if disk growth is regulated, e.g. via feedback. For example, Pezzulli, Fraternali & Binney (2017) describe gas accretion from a rotating hot corona gas in the halo. The accretion of such gas – with its associated angular momentum – is expected in a galactic fountain model in which stellar winds interact with the corona gas before falling back onto the disk. Such models explain the rotation lag of extraplanar gas in the Milky Way galaxy (Marinacci et al. 2011), and can help explain a slow growth in the size of the star-forming disk, strictly linked to the stellar disk size with small scatter.

Our results and modeling suggest that individual galaxies evolve almost parallel to the size-mass relation with a maximum evolution at $\frac{\mathrm{dlog}(r_e)}{\mathrm{dlog}(M_*)} \sim 0.26$ for $r_{e(SF)}/r_{e(M_*)} = 1.26$ (Figure 12), in agreement with the models from Nelson et al. (2019). The robustness of our measurement is also supported by comparisons to a completely independent estimate coming from expectations when comparing the sizes of Milky-Way progenitor galaxies selected at different redshifts assuming a constant cumulative co-moving number density ($\frac{\mathrm{dlog}(r_e)}{\mathrm{dlog}(M_*)} \sim 0.27$ from van Dokkum et al. 2013), and is slightly shallower than the slope ~ 0.3 discussed by van Dokkum et al. (2015) and ~ 0.4 for simulated galaxies with realistic wind models (Hirschmann et al. 2013). In contrast to models with no winds, the efficient removal of low angular momentum material at high redshift leads to much larger sizes for high redshift galaxies and shallower evolution, emphasising the role of feedback in the regulation of angular momentum in galaxies.

Some of the massive, star-forming $z = 2$ galaxies will have had their star-formation quenched by the time they reach $z = 1$. There are different theories of how such quenching proceeds and why it returns passive galaxies more compact than the coeval star-forming population: galaxies with low ($\lambda \lesssim 0.05$) spin parameters can become unstable and contract before rapidly being quenched (Dekel & Burkert 2014); galaxies reach a threshold stellar surface density, velocity dispersion, central surface density, stellar mass or bulge to total ratio before quenching (e.g. van Dokkum et al. 2015), or galaxies evolve along the main sequence and the effective quenching of massive galaxies is a gradual process, with older, earlier forming galaxies with higher density and smaller sizes departing first from the main sequence (Abramson & Morishita 2018; Lilly & Carollo 2016). Abramson & Morishita (2018) argue that the distribution of galaxies in the size-mass plane is not inconsistent with such a scenario in which galaxies evolve at constant surface mass density ($\frac{\mathrm{dlog}(r_e)}{\mathrm{dlog}(M_*)} = 0.5$). Our constraints show that such a steep evolution is only possible if the stellar sizes of galaxies grow via mechanisms other than star-formation. As shown – for very different models – by van Dokkum et al. (2015) and Abramson & Morishita (2018), such a strong apparent evolution can happen even if the evolution of individual galaxies is relatively weak, so long as the densest galaxies fall out of the star-forming population first and become passive. Our weaker measured star-formation driven evolution in size vs mass suggests that a more aggressive quenching is required, resulting in passive galaxies which are particularly dense and compact.

8. SUMMARY AND CONCLUSIONS

This paper utilises data from the KMOS^{3D} survey to measure the star-formation driven size growth in individual galaxies, and understand the physical processes driving this evolution at $0.7 \lesssim z \lesssim 2.7$, spanning the time when most of their stars were formed.

KMOS^{3D} targeted the Hα + [NII] emission line complex in 740 galaxies at $0.7 \lesssim z \lesssim 2.7$ with 75 nights of observation using the multiplexing NIR IFU instrument KMOS on the VLT. Datacubes and associated bootstrap cubes are released with an associated data release paper W19. In this paper we derive galaxy sizes in Hα emission, tracing ongoing star-formation. Our initial goal was to demonstrate the accurate measurement of galaxy half-light sizes with ground-based data at these redshifts, and in particular Hα sizes tracing star formation. With the investment of a significant calibration effort we have achieved our goal, with galaxy sizes measured with a typical accuracy of $\sim 20\%$, almost independent of the absolute size. Our analysis resulted in a sample of 281 galaxies for which we have accurate Hα size measure-

ments with associated errors. It is representative of the overall star-forming population in terms of SFR, stellar mass, colours and continuum size. We publish sizes and associated errors for this sample.

We then examined how the size of the star-forming gas, traced by Hα, relates to other galaxy properties. Our results can be summarized as follows:

- Hα sizes depend primarily on the continuum size of a galaxy, with a near-linear relation, a median (mean) Hα size = $r_{e(H\alpha)}$ $18 \pm 3\%$ ($\sim 26\%$) larger than $r_{e(r6500)}$, the continuum size at rest-frame 6500Å, with $43 \pm 3\%$ intrinsic log-normal scatter. This is much tighter than other correlations (e.g. $68 \pm 4\%$ intrinsic scatter in Hα size vs stellar mass) and explains most of the variation in Hα size. It is also smaller than the intrinsic scatter in continuum size vs stellar mass ($\sim 56\%$).

- The dependence of Hα size on continuum size shows no residual dependence on stellar mass, redshift, star-formation activity, galaxy morphology, or (indirectly) vs gas mass.

- There is a significant residual dependence of Hα size on dust extinction properties affecting the Hα emission. This dependence does not arise from the continuum extinction A_V. Instead, the size ratio depends primarily on the amount of extinction in the stellar birth clouds $A_{H\alpha}$ compared to A_V. For galaxies with larger Hα disks the ratio of these two extinction measurements tends to be lower, closer to a pure foreground screen approximation. This is in line with models suggesting that most obscuration of Hα emission far from galactic centres takes place in a diffuse, foreground component (equally affecting the continuum), while in galactic centres more obscuration of Hα is caused by dust embedded in HII regions (e.g. Li et al. 2019).

Based upon these results, we surmise:

- The tight correlation between the sizes of the star-forming and stellar components in star-forming, high redshift galaxies infers that the spin parameters of galaxies and their gas are tightly linked to the halo in which they live (see also Burkert et al. 2016), and are highly stable over long periods of cosmic time. Such stability not only requires stable halo growth but also stability in the transfer of specific angular momentum from halo to disk scales, including the processes of cooling, accretion, star-formation and feedback. Simulations and models suggest that feedback helps to modulate the disk growth (e.g. Hirschmann et al. 2013) and might help regulate the growth and its relation to the existing stars via galactic fountains (e.g. Pezzulli, Fraternali & Binney 2017). Such regulation applies consistently across a wide range of physical conditions as characterised by e.g. redshift, stellar or gas mass, star-formation rates, morphology, environment, and global extinction by dust, A_V.

- Star-formation drives size growth in galaxies, but is unlikely to evolve galaxies more steeply in size vs mass than the observed relation between those parameters at fixed redshift. We model this process including stellar mass loss. Excess dust extinction of Hα in galaxy centres means that our mean value of $r_{e(H\alpha)}/r_{e(F160W)} = 1.26$ is likely an upper limit on the size growth factor $r_{e(SF)}/r_{e(M_*)}$. A growth of $r_{e(SF)}/r_{e(M_*)} = 1.26$ moves galaxies along a locus with a slope $\frac{d\log(r_e)}{d\log(M_*)} \sim 0.26$, consistent with the slope of the mass-size relation and with the predicted evolution of Milky Way progenitors based on the observed sizes of galaxies selected at a constant cumulative co-moving number density in the Universe ($\frac{d\log(r_e)}{d\log(M_*)} \sim 0.27$ van Dokkum et al. 2013). A steeper evolution of the sizes of star-forming galaxies with mass, required to explain the roughly $H(z)^{-2/3}$ evolution in stellar sizes (vdW14), may be partially accommodated by accounting for the quenching of star-formation in the more compact galaxies (e.g. van Dokkum et al. 2015; Abramson & Morishita 2018) but likely requires other physical processes such as minor merging and angular momentum exchange with the halo.

REFERENCES

Abramson L. E., Morishita T., 2018, ApJ, 858, 40
Bigiel F., Leroy A., Walter F., Brinks E., de Blok W. J. G., MadoreB., Thornley M. D., 2008, AJ, 136, 2846
Bolatto A. D. et al., 2015, ApJ, 809, 175
Boselli A., Fossati M., Gavazzi G., Ciesla L., Buat V., Boissier S., Hughes T. M., 2015, A&A, 579, A102
Bouché N. et al., 2010, ApJ, 718, 1001
Brammer G. B. et al., 2012, ApJS, 200, 13
Burkert A. et al., 2016, ApJ, 826, 214
Calistro Rivera G. et al., 2018, ApJ, 863, 56
Calzetti D., Armus L., Bohlin R. C., Kinney A. L., Koornneef J., Storchi-Bergmann T., 2000, ApJ, 533, 682
Chang Y.-Y. et al., 2013, ApJ, 773, 149
Chen C.-C. et al., 2017, ApJ, 846, 108
Conroy C., Gunn J. E., White M., 2009, ApJ, 699, 486
Dalcanton J. J., Spergel D. N., Summers F. J., 1997, ApJ, 482, 659
Davies R. I., 2007, MNRAS, 375, 1099
Dekel A., Burkert A., 2014, MNRAS, 438, 1870
Dutton A. A., 2009, MNRAS, 396, 121
Erwin P., 2015, ApJ, 799, 226
Erwin P., Pohlen M., Beckman J. E., 2008, AJ, 135, 20
Fakhouri O., Ma C.-P., Boylan-Kolchin M., 2010, MNRAS, 406, 2267
Fall S. M., Romanowsky A. J., 2018, ApJ, 868, 133
Förster Schreiber N. M. et al., 2009, ApJ, 706, 1364
Förster Schreiber N. M. et al., 2006, ApJ, 645, 1062
Förster Schreiber N. M. et al., 2018, ApJS, 238, 21
Fossati M., Fumagalli M., Boselli A., Gavazzi G., Sun M., Wilman D. J., 2016, MNRAS, 455, 2028
Fossati M. et al., 2013, A&A, 553, A91
Fossati M. et al., 2017, ApJ, 835, 153
Fumagalli M., Fossati M., Hau G. K. T., Gavazzi G., Bower R., Sun M., Boselli A., 2014, MNRAS, 445, 4335
Gavazzi G. et al., 2015, A&A, 580, A116
Genzel R. et al., 2006, Nature, 442, 786
González Delgado R. M. et al., 2016, A&A, 590, A44
Grogin N. A. et al., 2011, ApJS, 197, 35
Hill A. R., van der Wel A., Franx M., Muzzin A., Skelton R. E., Momcheva I., van Dokkum P., Whitaker K. E., 2019, ApJ, 871, 76
Hirschmann M. et al., 2013, MNRAS, 436, 2929
Kassin S. A. et al., 2012, ApJ, 758, 106
Kelly B. C., 2007, ApJ, 665, 1489
Kelvin L. S. et al., 2012, MNRAS, 421, 1007
Kennicutt, Jr. R. C., 1998, ARA&A, 36, 189
Koekemoer A. M. et al., 2011, ApJS, 197, 36
Lang P. et al., 2017, ApJ, 840, 92
Lang P. et al., 2014, ApJ, 788, 11
Lelli F., McGaugh S. S., Schombert J. M., 2016, ApJ, 816, L14

Li H., Wuyts S., Lei H., Lin L., Lam M. I., Boquien M., Andrews B. H., Schneider D. P., 2019, ApJ, 872, 63
Lilly S. J., Carollo C. M., 2016, ApJ, 833, 1
Lilly S. J., Carollo C. M., Pipino A., Renzini A., Peng Y., 2013, ApJ, 772, 119
Livermore R. C. et al., 2015, MNRAS, 450, 1812
Madau P., Dickinson M., 2014, ARA&A, 52, 415
Marinacci F., Fraternali F., Nipoti C., Binney J., Ciotti L., Londrillo P., 2011, MNRAS, 415, 1534
Markwardt C. B., 2009, in Astronomical Society of the Pacific Conference Series, Vol. 411, Astronomical Data Analysis Software and Systems XVIII, Bohlender D. A., Durand D., Dowler P., eds., p. 251
McGrath E. J., Stockton A., Canalizo G., Iye M., Maihara T., 2008, ApJ, 682, 303
Mo H. J., Mao S., White S. D. M., 1998, MNRAS, 295, 319
Momcheva I. G. et al., 2016, ApJS, 225, 27
Nelson E. J. et al., 2019, ApJ, 870, 130
Nelson E. J. et al., 2012, ApJ, 747, L28
Nelson E. J. et al., 2016a, ApJ, 828, 27
Nelson E. J. et al., 2016b, ApJ, 817, L9
Newman A. B., Belli S., Ellis R. S., 2015, ApJ, 813, L7
Noeske K. G. et al., 2007, ApJ, 660, L43
Pastrav B. A., Popescu C. C., Tuffs R. J., Sansom A. E., 2013, A&A, 557, A137
Peng C. Y., Ho L. C., Impey C. D., Rix H.-W., 2010, AJ, 139, 2097
Pezzulli G., Fraternali F., Binney J., 2017, MNRAS, 467, 311
Saintonge A. et al., 2011, MNRAS, 415, 61
Schreiber C. et al., 2015, A&A, 575, A74
Sersic J. L., 1968, Atlas de Galaxias Australes
Skelton R. E. et al., 2014, ApJS, 214, 24
Storey P. J., Zeippen C. J., 2000, MNRAS, 312, 813
Stott J. P. et al., 2016, MNRAS, 457, 1888
Struck C., Elmegreen B. G., 2017, MNRAS, 469, 1157
Suess K. A., Kriek M., Price S. H., Barro G., 2019, ApJ, 877, 103
Tacconi L. J. et al., 2018, ApJ, 853, 179
Tacconi L. J. et al., 2013, ApJ, 768, 74
Tadaki K.-i. et al., 2017, ApJ, 834, 135
Toft S. et al., 2017, Nature, 546, 510
Turner O. J. et al., 2017, MNRAS, 471, 1280
van den Bosch F. C., 2001, MNRAS, 327, 1334
van der Wel A. et al., 2014a, ApJ, 792, L6
van der Wel A. et al., 2014b, ApJ, 788, 28
van der Wel A. et al., 2011, ApJ, 730, 38
van Dokkum P. G. et al., 2011, ApJ, 743, L15
van Dokkum P. G. et al., 2013, ApJ, 771, L35
van Dokkum P. G. et al., 2015, ApJ, 813, 23
Whitaker K. E. et al., 2014, ApJ, 795, 104
Williams R. J., Quadri R. F., Franx M., van Dokkum P., Labbé I., 2009, ApJ, 691, 1879
Wisnioski E. et al., 2019, ArXiv e-prints
Wisnioski E. et al., 2015, ApJ, 799, 209
Wisnioski E. et al., 2018, ApJ, 855, 97
Wuyts E. et al., 2016, ApJ, 827, 74
Wuyts S. et al., 2012, ApJ, 753, 114
Wuyts S. et al., 2013, ApJ, 779, 135
Wuyts S. et al., 2011, ApJ, 742, 96

ACKNOWLEDGMENTS

D.J.W. and M.F. acknowledge the support of the Deutsche Forschungsgemeinschaft via Projects WI 3871/1-1, and WI 3871/1-2. M.F. has received funding from the European Research Council (ERC) under the European Union's Horizon 2020 research and innovation programme (grant agreement No 757535). E.W. and J.T.M. acknowledges support by the Australian Research Council Centre of Excellence for All Sky Astrophysics in 3 Dimensions (ASTRO 3D), through project number CE170100013. PL acknowledges funding from the European Research Council (ERC) under the European Unions Horizon 2020 research and innovation programme (grant agreement No. 694343). G.B.B. acknowledges support from the Cosmic Dawn Center, which is funded by the Danish National Research Foundation. We thank the ESO and Paranal staff for the excellent support over the course of our KMOS observations. This work is also based on observations taken by the 3D-HST Treasury Program (GO 12177 and 12328) and by the CANDELS Multi-Cycle Treasury Program with the NASA/ESA HST, which is operated by the Association of Universities for Research in Astronomy, Inc., under NASA contract NAS5-26555.

APPENDIX

A. SIZE MEASUREMENTS: ACCURACY AND CONSISTENCY

The main goal of this paper is to present measurements of the size in Hα for KMOS^{3D} galaxies. With complimentary continuum measurements this provides the means to examine the spatial growth of high redshift galaxies via star-formation. This section provides a characterization and tests of the accuracy of our measurements with natural seeing KMOS data for both continuum and Hα.

In Figure 3 we have seen that our IMFIT -based sizes measured with the F160W WFC3 band are consistent with those measured by vdW14. Moreover, the right panel shows a remarkable consistency between our higher resolution WFC3 sizes and those derived from the KMOS continuum.

A.1. *Definition of Galaxy Size Errors*

The accuracy of measured half-light size of galaxies is sensitive to sources of noise (systematic and random), and to the spatial resolution.

Our bootstrap cubes randomly sample most sources of systematic and random noise, so we use these to assess asymmetric $1-\sigma$ errors in size. **Bootstrap size errors** encompass the range between the 16^{th} and 84^{th} percentiles of the sizes measured from the bootstrap cubes.

In some cases the median size measured from the bootstrap cubes differs from the size measured using our total combine cube. To be conservative, we also define **statistical size errors** such that the negative and positive errors are each the maximum of the difference between the median bootstrap or total combine, and the 16^{th} and 84^{th} bootstrap percentiles respectively.

Sizes based on the bootstrap cubes do not account for any uncertainty on the PSF. Therefore in Section A.4 we assess the impact of PSF uncertainty on galaxy size measurements, assigning a minimum size error based on the uncertainty due to the PSF. Our **final size errors** are the maximum of the statistical errors, and this minimum error based on the PSF uncertainty.

In the following discussion we shall examine our bootstrap, statistical and final errors. Our final results use final errors in all cases.

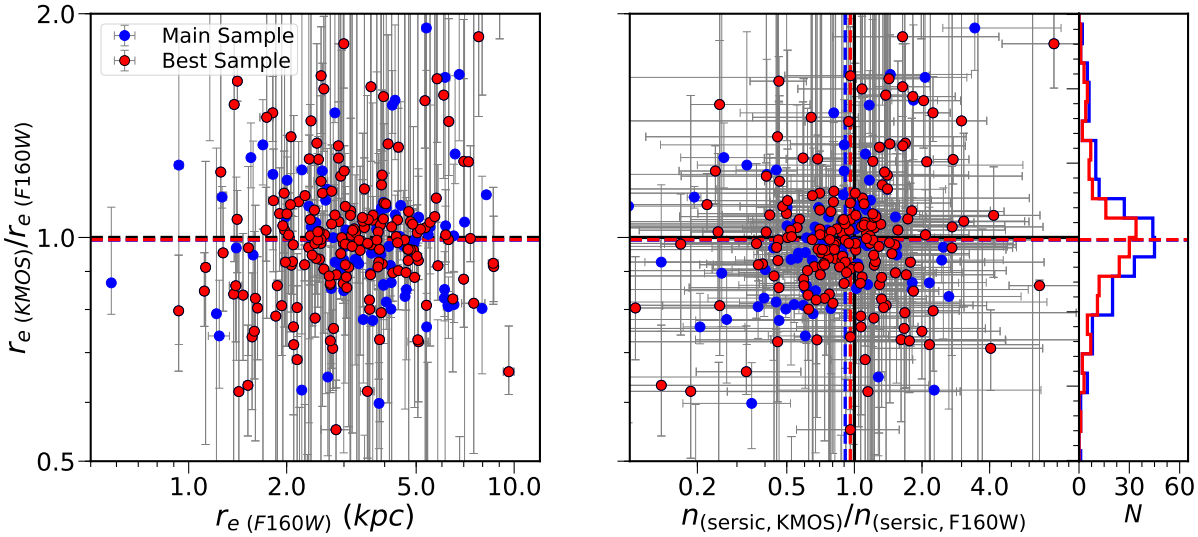

Figure A1. Left: Ratio of KMOS continuum based effective radius (r_e) to that from CANDELS (F160W), as a function of the CANDELS F160W r_e for galaxies in the continuum MAIN (blue) and BEST (red) samples, and its distribution (narrow panel to right). Errors on the size ratio are derived from bootstrap errors on KMOS continuum sizes. The median ratio is 0.99 for both samples (dashed horizontal lines) and does not notably depend upon the galaxy size, demonstrating the well recovered continuum sizes of galaxies from KMOS data. Right: Compares the ratio of parameters – size (r_e) and Sersic index (n_{Sersic}) – from fitting to the KMOS continuum data to those from fitting the CANDELS F160W-band images, with bootstrap error bars, and their medians (horizontal and vertical dashed lines). Both parameters are well reproduced with fits to the KMOS continuuum data. Galaxies are divided into the continuum MAIN and BEST samples.

A.2. *Errors on Galaxy Sizes: Continuum*

We now examine the accuracy of KMOS continuum sizes, assessed via comparison with the higher resolution sizes measured on CANDELS WFC3 data. In the left panel of Figure A1, we find that the galaxy sizes fit to the KMOS continuum image are equivalent to those from fits to the higher resolution and signal to noise CANDELS F160W-band images, with a median offset of just 1% for both continuum MAIN and BEST samples, and no apparent dependence on galaxy size. The right panel extends this to the joint parameter space of size and Sersic index: Sersic indices are also compatible, with median offsets of $< 10\%$.

Figure A2 examines the distribution of these size offsets compared to our derived errors. In the top-left panel we show the cumulative distribution of size offsets normalized by the size itself ($\frac{r_e(KMOS) - r_e(F160W)}{r_e(F160W)}$) and of our estimated size errors, also normalized by size. We measure more small fractional offsets in size than would be predicted by our measurement errors, suggesting some errors are slightly overestimated. This is mostly due to the difference between bootstrap and statistical errors – i.e. to account for differences between the median bootstrap realisation and the best estimate. The top-right panel examines this fractional (final) error and offset distribution separately for the most compact galaxies ($r_e < 2$ kpc) and for more extended galaxies, demonstrating little difference in the accuracy of sizes or of size errors, perhaps because compact sources tend to be brighter, compensating for the lack of resolution with higher signal to noise. In the bottom-left panel the size offsets are normalized by the size error. Especially using our final errors, this describes something very close to an error function with a dispersion of 1 and median of 0, as would be expected in the case that the errors are accurate. Therefore we consider our size errors (at least for KMOS continuum sizes) to be well calibrated.

A.3. *Errors on Galaxy Sizes:* Hα

The bottom-right panel of Figure A2 now examines the errors for both KMOS continuum sizes and KMOS-based Hα sizes. This shows the cumulative distribution of fractional errors on KMOS continuum and Hα sizes, from the respective MAIN samples and divided into compact and extended sub-samples (at 2 kpc).

While the error distribution for KMOS continuum and Hα is very similar for extended sources, the compact Hα galaxies have significantly smaller errors than the compact KMOS continuum galaxies.

We have shown that the errors on the KMOS continuum sizes are well described by (systematic and random) signal to noise variations as traced primarily by the bootstrap errors. Figure A2 demonstrates that the compact (typically high signal-to-noise) Hα sources can have very small size errors. This motivates a more thorough examination of the effects of uncertainty on the PSF in Section A.4, resulting in the final size errors. We note here, based on a comparison of bootstrap / statistical, and final errors in Figure A2, that this inflates the smallest size errors for compact galaxies, but that there are nonetheless fewer compact galaxies with large fractional size errors in Hα than for extended galaxies or for KMOS continuum, implying that this is robust and likely a consequence of the high signal to noise data. We also tested the impact of our choice of a flat extension of the velocity field beyond the regions where we trust kinematic

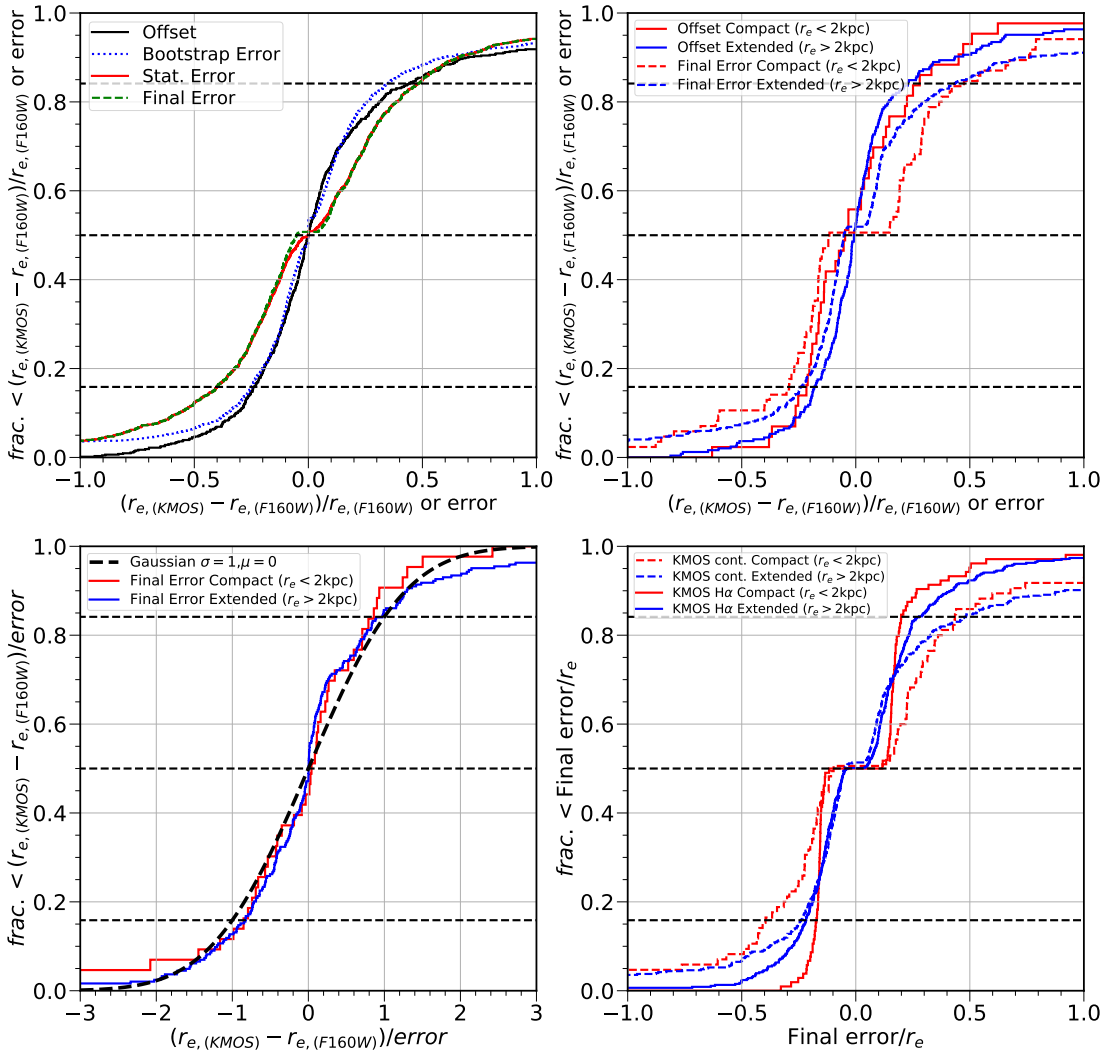

Figure A2. **Top left:** Cumulative distribution of the relative difference (offset) between KMOS continuum and CANDELS F160W based size measurements ($\frac{\mathrm{r_e(KMOS)-r_e(F160W)}}{\mathrm{r_e(F160W)}}$, solid black line) from the continuum MAIN sample. This is compared to the cumulative distribution of the expected size error distribution for these galaxies: we show bootstrap (dotted), statistical (dashed) and final (solid) error distributions (see Section A.1 for error definitions). **Top right:** Offsets and final error cumulative distributions, divided into compact (red) and extended (blue) sources at $\mathrm{r_e} = 2\,\mathrm{kpc}$. Remarkably, fractional offsets are similar for compact and extended galaxies, and while the final error (which accounts for PSF uncertainty) inevitably gives larger fractional errors for compact galaxies, this converges to similar values for larger fractional errors.

Bottom Left: Cumulative distribution of the error-normalized size offset: $\frac{\mathrm{r_e(KMOS)-r_e(F160W)}}{\sigma(\mathrm{r_e(KMOS)-r_e(F160W)})}$ again divided into compact and extended sources at $\mathrm{r_e} = 2\,\mathrm{kpc}$. Galaxies offset negatively from their F160W sizes are normalized by the negative error and vice versa. With accurate errors, this should descibe a normal distribution with a mean of 0 and scatter of 1, the cumulative version of which is the equivalent error function (black dashed-line). This provides a remarkably good match to both compact and extended sources, indicating that our final errors are accurate, not a function of size, and applicable to galaxies sampled with KMOS resolution with our best guess KMOS PSF. **Bottom Right:** Cumulative distribution of fractional (final) size errors for KMOS continuum and Hα, selected respectively from the continuum MAIN and Hα MAIN samples, and divided into compact and extended galaxies at $\mathrm{r_e} = 2\,\mathrm{kpc}$ (independently for KMOS continuum and Hα measurements). While the relative errors on KMOS continuum sizes are slightly larger for compact galaxies, the opposite is true for the Hα case: compact galaxies have smaller relative errors on average.

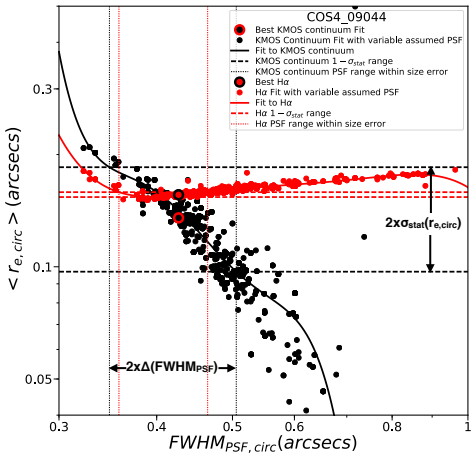

Figure A3. Best fit circularized effective radius, $< r_{e,circ} >$ expressed in angular units, for compact galaxy COS4_09044 in KMOS continuum (black) and Hα (red) as a function of the FWHM of the circularized PSF ($FWHM_{PSF,circ}$) which is assumed for the fit (to the same data). The fit with the best guess PSF for this galaxy is indicated with the larger, outlined datapoints. With a larger PSF, the best fit size to KMOS continuum data decreases to compensate. This is representative of the typical behaviour for most galaxies. Only if the assumed PSF is well away from our best guess will the fit to the KMOS continuum data provide a best fit galaxy size outside the range allowed by the statistical errors from bootstrap cubes (dashed horizontal black lines) which samples random and systematic variations in the input data. We fit the trend with a fifth order polynomial including sigma-clipping (black solid line) and measure the range of assumed $FWHM_{PSF,circ}$ accommodated within the statistical errors (black dotted vertical lines, the separation of which is defined to be $2 \times \Delta FWHM_{PSF,circ}$). The H$\alpha$ fits, in contrast, provide a very stable circularized galaxy size *almost independent of bootstrap iteration* (red dashed horizontal lines) *or of the assumed PSF* (lack of variation with $FWHM_{PSF,circ}$, fit indicated as the red solid line). This is typical of high signal to noise Hα data for compact galaxies (r_e(Hα) $\lesssim 0.25''$ or 1.25 pixels) as seen in Figure A4.

fits in individual spaxels. We modified the velocity in these extrapolated regions to values 25% above and below the nominal values. Thsi simulates either declining rotation curves at large radii (Lang et al. 2017), or rotation curves that keep raising to larger velocities. The impact on the final Hα sizes is negligible, with a scatter with respect to the best values of 1-2% in both our tests. This scatter is much smaller than the individual measurements errors, which are therefore not affected by the algorithm used to extend the velocity fields.

A.4. *Effects of PSF Uncertainty on Size Errors*

As described in Section 3.2, the generation of PSF images for each combined cube relies on our ability to accurately measure the shifts between exposures, acquisitions and setups, as characterised via the simultaneously observed stars, and shifts between partial combines. An uncertainty on the PSF (e.g. from arm positioning errors not accounted for via shifts between partial combines) translates to a limit to our effective size or size error estimates which is not accounted for by the bootstrap errors, but which must be smaller than the typical error on the KMOS continuum size (given those bootstrap errors are large enough to describe the offset from CANDELS based sizes, Section A.2).

To examine how the size estimates are sensitive to the assumed PSF, we refit every galaxy in the sample with the PSF (image) as computed for all of the other galaxies in the sample. This covers a much broader range of PSF than any realistic, residual error on the true PSF. Figure A3 shows the resultant variation of best fit galaxy half-light radius with assumed PSF (circularized) FWHM for one of our compact galaxies, COS4_09044. The dependence on the size of the PSF is most closely related to the circularised size, $r_{e,circ}$, expressed in angular units (arcseconds)[30].

Focusing on the results for the fit to the KMOS continuum (black points), we see the expected trend as typically seen for most galaxies (including more extended ones): as a larger PSF is assumed, the fitting procedure compensates such that the best fit intrinsic galaxy size is more compact. To illustrate the range of assumed PSF which can be accommodated within the $1-\sigma$ size range derived using the statistical errors from the bootstrap cubes dashed black horizontal lines – i.e. the range of PSF for which the statistical errors dominate over any size error induced by the assumption of the incorrect PSF – we fit the dependence of predicted galaxy size on assumed PSF FWHM with a fifth order polynomial (green solid line, fit is iterative with sigma-clipping) and determine the range of PSF FWHM for which this fit lies within the statistical errors on size (dotted vertical black lines), with a full range $2 \times \Delta FWHM_{PSF,circ}$.

In Figure A4 we show how $\Delta FWHM_{PSF,circ}$ depends upon the statistical error range of the galaxy size ($\sigma_{stat}(r_{e,circ})$ in arcseconds, the average of positive and negative errors). $\Delta FWHM_{PSF,circ}$ saturates at a maximum value, corresponding to the full range of $FWHM_{PSF,circ}$. For smaller size errors, there exist some range of assumed PSF which would drive the galaxy size outside the statistical error: the range of PSF consistent with the measured size and statistical errors becomes smaller with decreasing statistical error along a locus of slope ~ 0.9 (a power law on linear scales with exponent 0.9). Repeating the exercise for Hα fits (red points in Figures A3 and A4) we see that for most

[30] Circularized sizes are defined as $r_{e,circ} = r_e.\sqrt{1-\epsilon}$, $FWHM_{PSF,circ} = FWHM_{PSF,major}.\sqrt{1-\epsilon_{PSF}}$.

KMOS^{3D} ID	KMOS^{3D} ID TARGETED	z_{spec}	$r_{e\ (F160W)}$ (kpc)	$\sigma(r_{e\ (F160W)})$ (kpc)	$r_{e\ (H\alpha)}$ (kpc)	$\sigma_{neg.}(r_{e\ (H\alpha)})$ (kpc)	$\sigma_{pos.}(r_{e\ (H\alpha)})$ (kpc)
(1)	(2)	(3)	(4)	(5)	(6)	(7)	(8)
COS4_06327	COS3_06511	0.80364	2.458	0.034	3.803	0.453	0.842
GS4_34568	GS4_34568	2.57255	3.845	0.071	5.125	0.612	0.940
U4_09733	U4_09733	2.28886	3.931	0.092	11.243	1.051	1.170
.....							

Table C1
Example of the size measurements table made available with this work.

Notes.

- (1) KMOS^{3D} ID : Object ID as defined in the data release (W19).
- (2) KMOS^{3D} ID TARGETED : the object ID that defined the target at the time of the observations as defined in W19. In this paper we refer to these IDs.
- (3) Spectroscopic redshift based on KMOS^{3D} emission line detection.
- (4) $r_{e\ (F160W)}$ effective radius from WFC3/F160W images in kpc.
- (5) $\sigma(r_{e\ (F160W)})$ symmetric 1σ uncertainty on the effective radius from WFC3/F160W images in kpc.
- (6) $r_{e\ (H\alpha)}$ effective radius from KMOS Hα images in kpc. The flux image is derived as described in equation 4.
- (7) $\sigma_{neg.}(r_{e\ (H\alpha)})$ asymmetric negative 1σ uncertainty on the effective radius from KMOS Hα images in kpc. The final error as defined in Appendix A.
- (8) $\sigma_{pos.}(r_{e\ (H\alpha)})$ asymmetric positive 1σ uncertainty on the effective radius from KMOS Hα images in kpc. The final error as defined in Appendix A.

cases (in particular for galaxy sizes $r_e \gtrsim 0.25''$) the data follow the same trend, for which we perform a linear fit (green solid line in Figure A4).

We estimate that there can exist a *maximum* residual error of $\sim$ 1pixel $= 0.2''$ on $FWHM_{PSF,circ}$, as a result of uncertain manual shifts between partial combines, and residual errors after the average exposure to exposure shift of PSF stars has been removed. This sets a conservative upper limit on the error on $FWHM_{PSF,circ}$ for a compact PSF ($FWHM_{PSF,circ} \sim 0.4''$) of $\sim \sqrt{(0.4'')^2 + (0.2'')^2} - 0.4'' \sim 0.05''$. We assume that where $\Delta FWHM_{PSF,circ} < 0.05''$ (horizontal dashed black line, Figure A4) the PSF error overrides the statistical error: this sets a lower limit on the final error on the size at the point where our locus of points (green line) intersects this limiting value of $\Delta FWHM_{PSF,circ}$, such that our final error on circularized galaxy size, $\sigma(r_{e,circ}) \geq 0.025''$ (vertical dashed black line, $= \frac{1}{8}$ of a pixel).

For the fits to compact galaxies in Hα ($r_e < 0.25''$), the statistical errors on size from the bootstraps are often very small, $\sigma_{stat}(r_{e,circ}) < 0.01''$ or < 0.05 pixels and with a much shallower dependence of best fit size on assumed PSF (and thus larger value of $\Delta FWHM_{PSF,circ}$ at fixed $\sigma_{stat}(r_{e,circ})$). A good example is COS4_09044, highlit in blue in Figure A4, for which the Hα fit provides a extremely consistent size almost independent of the bootstrap iteration or the assumed $FWHM_{PSF,circ}$ (red points in Figure A3). Such galaxies are high signal to noise and high surface brightness (surface brightness increases with decreasing size), but the best correlation is with size: the residuals with respect to the main locus in Figure A4 are plotted against galaxy size in the upper panel. We conservatively set the errors of all such fits to our adopted minimum value of $\sigma(r_{e,circ}) \geq 0.025''$ (vertical dashed black line). Most galaxies, especially in the case of KMOS continuum have larger statistical errors and so these error estimates remain effectively consistent with the differences between KMOS continuum and CANDELS sizes. We now define the **final size errors** on (major axis) sizes, $\sigma(r_e)$, to be the maximum of the statistical error and the uncertainty on size due to the PSF uncertainty of $0.025'' \times \sqrt{1-\epsilon} \times D_A$ where D_A is the angular diameter distance at the redshift of the galaxy in kpc arcsec^{-1}.

Finally we note that there are no fits to Hα data which are flagged as OK for which best fit sizes are below $r_e \sim 0.69$ pixels. This seems to be the real limit for galaxy Hα sizes in our sample as there is no reason that smaller sizes should be flagged as bad (even if perfectly described by the PSF). This corresponds to a minimum physical size of $r_e \sim 1.1$ kpc, very similar to the minimum size from CANDELS F160W continuum imaging (Figure 3). In contrast, a few KMOS continuum sizes reach to both much lower and larger sizes (as seen in Figure 3): these can be explained as outliers, and are mostly consistent with the tails in the difference between KMOS continuum and CANDELS F160W sizes, normalized by the size errors: i.e. they are mostly expected given the errors, with a few possible exceptions.

B. EXAMPLES OF Hα PROFILES AND EXPONENTIAL FITS

In Figure B1 we show a gallery of Hα profiles from the MAIN sample spanning a range of size, redshift and observed surface brightness, to show the quality of the data and of the fitting procedure.

C. PUBLIC RELEASE OF SIZE MEASUREMENTS

The size measurements of 281 galaxies in the Main Sample are made available as a Machine Readable Table. Table C1 gives an example of the quantities provided with this work and the description of the columns:

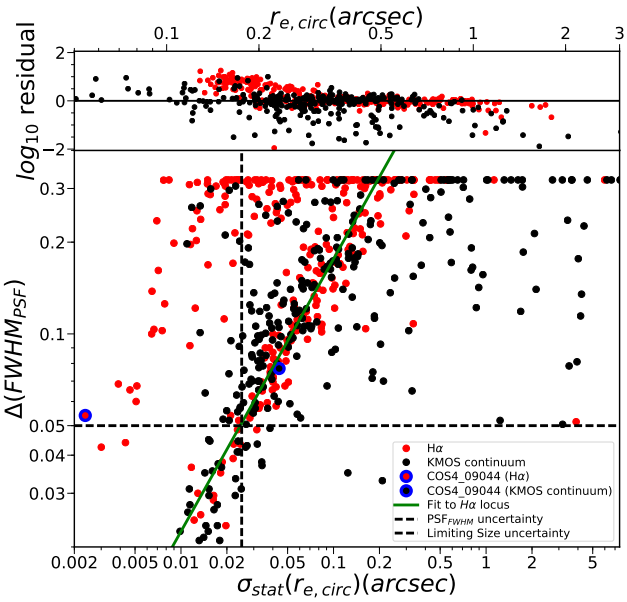

Figure A4. Each galaxy is fit with the full range of assumed PSF, as described in Section A and illustrated by Figure A3. The *statistical* error on galaxy size, $\sigma_{\rm stat}({\rm r_e})$ is estimated using the fits to bootstrap cubes. Here the statistical error on circularized galaxy size, $\sigma_{\rm stat}({\rm r_{e,circ}})$, is shown plotted aginst the half-range of PSF circularized FWHM, $\Delta{\rm FWHM_{PSF,circ}}$, for which the best fit galaxy size lies within the statistical error (i.e. the range of PSF error for which the statistical error dominates the error on the assumed PSF). All galaxies in the continuum MAIN (black, KMOS continuum) and Hα MAIN (red) are shown. The vast majority of galaxies in KMOS continuum, and many in Hα, lie along a locus of decreasing $\Delta{\rm FWHM_{PSF,circ}}$ with decreasing $\sigma_{\rm stat}({\rm r_{e,circ}})$ (solid green line) – such that for very small statistical size errors the error on assumed PSF can dominate. As described in the main text we assume a conservative error on the assumed PSF of $\Delta{\rm FWHM_{PSF,circ}} = 0.05''$ (horizontal dashed black line), for which the error is matched by a statistical error of $\sigma_{\rm stat}({\rm r_{e,circ}}) = 0.025''$, or $\frac{1}{8}$ of a KMOS pixel (vertical dashed black line). At very compact sizes, ${\rm r_{e,circ}} \lesssim 2.5''$, the statistical error on Hα sizes becomes very small, and the sensitivity to $\rm FWHM_{PSF,circ}$ becomes quite flat, as seen in Figure A3 for COS4_09044. These galaxies are to the left of the main locus of points in this Figure, and are clearly shown with positive residuals in the upper panel in which we show the residual of $\Delta{\rm FWHM_{PSF,circ}}$ with respect to the Hα locus versus galaxy size. We choose to apply a conservative lower limit to the circularized galaxy size error, $\sigma({\rm r_{e,circ}}) \geq 0.025''$, corresponding to the vertical dashed line.

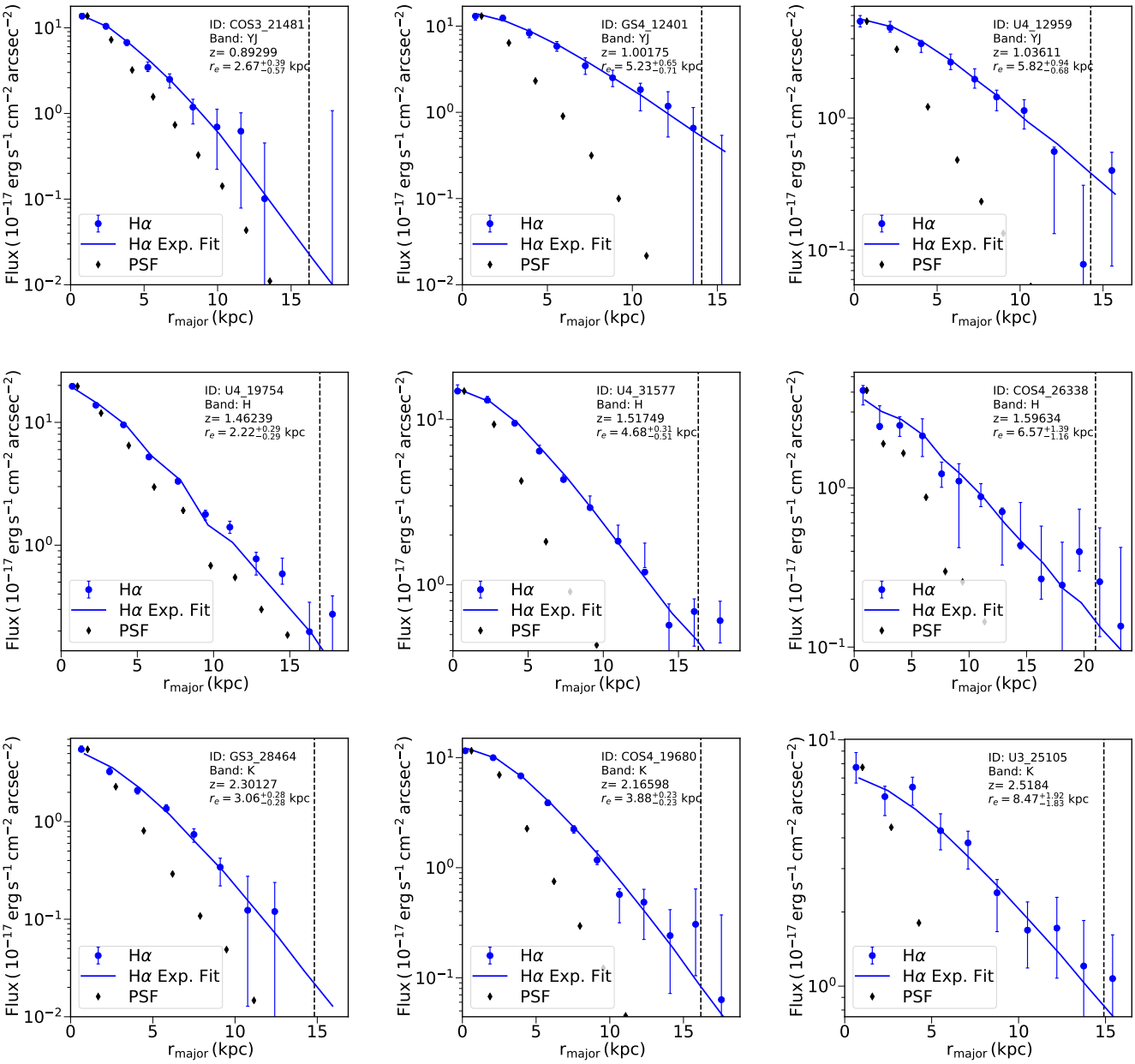

Figure B1. Gallery of radial Hα profiles extracted using elliptical apertures from our KMOS data (blue points with 1σ bootstrap errors) as described in Section 4. The blue solid lines show the 1D profiles of the best fit 2D exponential model. For comparison the PSF image is also extracted in the same apertures (black diamonds). The vertical dashed line indicates the radius where the major axis first crosses the edge of the KMOS field of view. The galaxies have increasing effective radii from the left to the right column, while the galaxy redshift increases from top to bottom.